CFD analysis of the full-scale resistance of an oil tanker in presence of a mud–water interface

Lovato, S.; Toxopeus, S.L.; Settels, J.W.; Keetels, G.H.; Kirichek, A.

DOI
10.1016/j.oceaneng.2024.116700

Publication date
2024

Document Version
Final published version

Published in
Ocean Engineering

Ocean Engineering 294 (2024) 116700

Contents lists available at ScienceDirect

Ocean Engineering

journal homepage: www.elsevier.com/locate/oceaneng

CFD analysis of the full-scale resistance of an oil tanker in presence of a mud–water interface

S. Lovato [c], S.L. Toxopeus [c], J.W. Settels [c], G.H. Keetels [a], A. Kirichek [b,*]

[a] Section of Offshore and Dredging Engineering, Department of Maritime and Transport Engineering, Faculty of Mechanical, Maritime and Materials Engineering, Delft University of Technology, Leeghwaterstraat 2, 2628 CA Delft, The Netherlands

[b] Section of Rivers, Ports, Waterways and Dredging Engineering, Department of Hydraulic Engineering, Faculty of Civil Engineering & Geosciences, Delft University of Technology, Stevinweg 1, 2628 CN Delft, The Netherlands

[c] Maritime Research Institute Netherlands, P.O. Box 28, Wageningen 6700AA, The Netherlands

ARTICLE INFO

Keywords:
Shallow water
CFD
KVLCC2
Nautical bottom
Mud rheology
Yield stress

ABSTRACT

The presence of mud layers on the bottom of ports and waterways can have negative effects on the hydrodynamic behaviour of marine vessels. This numerical study investigates the effect of muddy seabeds on the full-scale resistance of an oil tanker sailing straight ahead. The objective is to determine the influence of factors such as the densimetric Froude number, UKC and mud rheology at speeds between 3 and 9 knots. The numerical study is conducted using a finite-volume Reynolds-Averaged Navier–Stokes (RANS) flow solver combined with the Volume-Of-Fluid (VOF) method to capture the mud–water interface. At certain critical speeds, the presence of mud increased the ship's total resistance by up to 15 times compared to the case with solid bottoms. The non-Newtonian rheology of mud was found to influence the ship's resistance mainly at low speeds and when sailing through the mud layer. This article also shows that, when sailing through mud, the computed resistance at high speeds may be underestimated because of two effects, namely 'water lubrication' and 'numerical ventilation'.

1. Introduction

When sailing in confined waters, ships must maintain a minimum under-keel clearance (UKC) with respect to the bottom of a fairway in order to ensure sufficient manoeuvrability. The presence of fluid mud layers in the channels leads to a net reduction of the UKC, although a quantitative estimate of such reduction is difficult to make as the definition of "bottom" and "depth" becomes less obvious. This raises questions on the amount of mud that needs to be dredged to ensure safe navigation while minimising costs.

A balance between costs and safety can be better identified using the concept of "nautical bottom", which is defined by PIANC (McBride et al., 2014) as *"the level where physical characteristics of the bottom reach a critical limit beyond which contact with a ship's keel causes either damage or unacceptable effects on controllability and manoeuvrability"*. In practice, port authorities define the nautical bottom as the level where the mud reaches either a critical density or a critical strength (yield stress) (McAnally et al., 2007). However, according to its definition, an optimal implementation of the nautical bottom concept would also require a good understanding of the ship's behaviour in relation to the physical characteristics of mud.

The most substantial research effort to better understand ship-mud interaction was done on scaled models. Between 1976 and 1989, experiments have been conducted at the Netherlands Ship Model Basin (currently MARIN, Sellmeijer and van Oortmerssen, 1984), Flanders Hydraulics (Belgium, Vantorre and Coen, 1988; Van Craenenbroeck et al., 1992; Vantorre, 1994) and SOGREAH (France, Brossard et al., 1991), where the mud layer was simulated using clay suspensions or mineral oil. A more comprehensive series of captive model tests were later carried out at Flanders Hydraulics using paraffin oil to mimic the mud layer (Delefortrie et al., 2005). Based on these tests, a manoeuvring model was derived and used in a ship manoeuvring simulator (Delefortrie et al., 2007).

In general terms, it was found that the presence of mud alters the hull forces because of two main effects. The first stems from the high viscosity of mud, which tends to increase the viscous forces in case of contact with the hull. The second effect can occur even without contact and is due to the generation of internal waves on the mud–water interface. When sailing close to critical speeds, these waves can significantly alter the pressure distribution on the hull and therefore the resistance and the manoeuvring behaviour. This effect is analogous

* Corresponding author at: Section of Rivers, Ports, Waterways and Dredging Engineering, Department of Hydraulic Engineering, Faculty of Civil Engineering & Geosciences, Delft University of Technology, Stevinweg 1, 2628 CN Delft, The Netherlands.

E-mail addresses: s.lovato@marin.nl (S. Lovato), o.Kirichek@tudelft.nl (A. Kirichek).

https://doi.org/10.1016/j.oceaneng.2024.116700
Received 10 August 2023; Received in revised form 26 December 2023; Accepted 11 January 2024
Available online 19 January 2024

to the "dead-water phenomenon" reported in 1893 by Nansen (2008) during an expedition to the North Pole and later studied experimentally by Ekman (1904). In that case, the dead-water effect was attributed to internal waves occurring at the interface between fresh and salt water, which led to a noticeable increase in the ship's resistance. Further references on the dead-water phenomenon can be found e.g. in Miloh et al. (1993), Esmaeilpour et al. (2018), Mercier et al. (2011) and Grue (2015) and in the references therein.

The ship's behaviour observed in model-scale experiments with muddy bottoms was qualitatively confirmed by full-scale trials, carried out in the harbour of Rotterdam (Netherlands, Van Bochove and Nederlof, 1978), Delfzijl (Netherlands, Verwilligen et al., 2014; Barth et al., 2016) and Zeebrugge (Belgium, Van Craenenbroeck et al., 1992). The problem has also been investigated using theoretical approaches based on potential flow (Miloh et al., 1993; Miloh, 1995; Doctors, 1996; Zilman and Miloh, 1995; Zilman et al., 1996). More recently, potential-flow simulations of the KVLCC2 sailing above muddy seabeds were performed (Sano and Kunitake, 2018), which confirmed the steep increase in resistance when sailing at critical speeds. With the increasing power of today's computers, viscous-flow calculations using Computational Fluid Dynamics (CFD) have become within reach of application, allowing to account for the viscous effects that are neglected by the less computationally expensive potential-flow solvers.

This article investigates the effect of muddy bottoms on the ship's resistance using CFD. The first documented CFD study on the subject investigated the resistance of the Wigley hull, modelling the mud layer as a non-Newtonian fluid using the Herschel–Bulkley model (Gao et al., 2015). (For a comprehensive overview of non-Newtonian fluid models and rheology, refer to specialised textbooks such as Chhabra and Richardson (2008) and Irgens (2014)) Another CFD study was later carried out to investigate the effect of muddy bottoms on the resistance, sinkage and trim of a model-scale container vessel (Kaidi et al., 2020). In their study, the mud layer was modelled as a Newtonian fluid since little difference was observed when using a non-Newtonian model such as Bingham. More recently, flow around KVLCC2 at model scale has been simulated with CFD and a steep increase of the resistance has been observed when sailing at critical speeds (Leijs, 2021). Finally, CFD has also been recently used to calculate the effect of mud on the drag of simpler geometries like plates (Lovato et al., 2022b) and cylinders (Sotelo et al., 2023). This allowed validation against relatively simpler and more controlled experiments as compared to ship-model tests with mud.

This work differs from the previous numerical studies in two key aspects. Firstly, CFD simulations are performed at full scale, eliminating the need for scaling the mud properties. Secondly, the effect of the mud rheology on the ship's resistance is discussed in more detail and for a wider range of speeds and mud layer characteristics. The mud layer is modelled as a Bingham fluid, which enables to capture its yield-stress behaviour.

The effect of muddy bottoms on the full-scale resistance of KVLCC2 is numerically investigated at speeds between 3 and 9 knots, which is a representative range for navigation in shallow waters. The study is conducted using a finite-volume Reynolds-Averaged Navier–Stokes (RANS) flow solver combined with the Volume-Of-Fluid (VOF) method to capture the mud–water interface. Some difficulties that may arise when simulating this type of conditions are illustrated and possible strategies to mitigate them are discussed.

The article is structured as follows. Section 2 describes the problem investigated in this article and provides information about the geometry of the simulated ship. Section 3 describes the equations that govern the problem and that are solved by the CFD solver in discretised form, whereas the simulated test cases are listed in Section 4. The computational setup, including the grids and the boundary conditions, is described in detail in Section 5. The results are discussed in Section 6, which is divided in three subsections. In the first, the numerical uncertainties are estimated both for solid and muddy bottoms by performing grid refinements. Results with solid bottoms are also compared with literature data. In the second subsection, the influence of numerical effects on the resistance are discussed, including numerical ventilation, water lubrication, the regularisation parameter, the use of wall functions and the interpolation method for the viscosity. The last subsection of Section 6 discusses the effect of the mud layer on the resistance caused by the internal wave and by the rheology of mud. Finally, the conclusions and recommendations are summarised in Section 7.

Table 1
Main particulars of KVLCC2.

Particular	Symbol	Value	Unit
Length p.p.	L	320	m
Beam	B	58	m
Draught	T	20.8	m
Hull wetted area	S	27,713	m^2
Block coefficient	C_B	0.81	–

2. Problem formulation and ship geometry

The problem is schematically illustrated in Fig. 1 and it consists in the bare hull (no appendages) of a modern tanker moving forward in shallow waters, with a fixed depth-to-draught ratio, h/T, equal to 1.5. On top of the flat solid bottom there is a fluid mud layer having thickness h_m, laying underneath a water layer h_w. The under-keel clearance (UKC) is relative to the mud-water interface and will be given as a percentage of T throughout the article. Note that with $h/T = 1.5$ and negative UKC, the resulting mud layer may become unrealistically thick for typical harbour navigation. However, the intention of this study is not to reproduce specific harbour conditions, but rather to illustrate both the general effects of the mud layer on the bare-hull resistance and the possible difficulties that may arise when studying this problem with CFD, regardless of the specific channel depth.

In order to generalise the problem, a laterally unbounded domain is considered. The origin of the Cartesian reference frame is at the intersection of the symmetry plane with the keel line and the aft perpendicular. The x-axis is aligned with the ship moving direction, while the y-axis and the z-axis point portside and upwards, respectively.

The configuration is fully captive, hence dynamic trim and sinkage are not considered. Furthermore, as the disturbance of the air–water free surface for displacement ships is typically rather small, the free surface is approximated as a frictionless rigid lid. While these may be sensible assumptions, the effect of trim and sinkage and of the free surface are deemed of secondary importance for this study, as the focus is on the effect of mud on the resistance at relatively low speeds. A study on ship-bank interaction (Van Hoydonck et al., 2019) also showed that there is no clear trend indicating that the use of trim, sinkage and free surface leads to resistance predictions closer to measurements.

The ship under investigation is the KVLCC2 (Hino, 2005), a type of Very Large Crude Carrier (VLCC) ship widely used as benchmark for experimental and numerical studies (see e.g. Larsson et al., 2003). The geometry is the same as used in Pereira et al. (2017) (Fig. 2), which is a modification of the original KVLCC2 by fairing the transom as in Fig. 3. This avoids complications due to possible unsteady vortex shedding and strong flow separation near the air–water interface. The main particulars of KVLCC2 are reported in Table 1. The CAD file of the hull is available as "supplementary material".

3. Mathematical model

3.1. Continuity and momentum

The isothermal, turbulent and incompressible flow around KVLCC2 is simulated by solving the following Reynolds-averaged Navier–Stokes

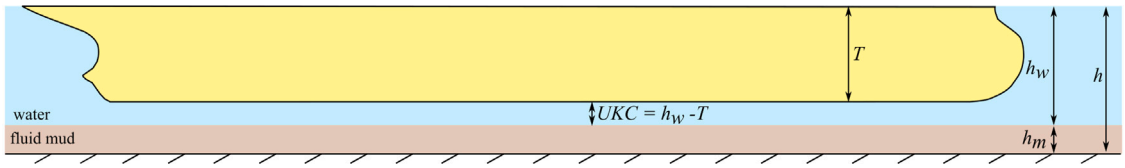

Fig. 1. Schematic representation of a ship sailing is shallow water ($h/T = 1.5$ in this work) with a muddy bottom.

Fig. 2. Starboard side view of KVLCC2 (with faired transom).

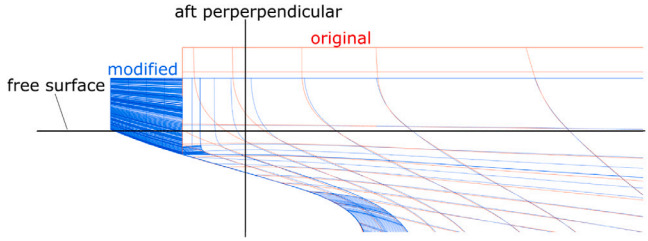

Fig. 3. Modification of the original KVLCC2.

(RANS) continuity and momentum equations:

$$\nabla \cdot \boldsymbol{u} = 0 \tag{1}$$

$$\frac{\partial(\rho \boldsymbol{u})}{\partial t} + \nabla \cdot (\rho \boldsymbol{u}\,\boldsymbol{u}) = \nabla \cdot \left(2\mu \boldsymbol{S} + \boldsymbol{\tau}^{\boldsymbol{R}}\right) - \nabla p + \rho \boldsymbol{g} \tag{2}$$

where $\boldsymbol{u}(\boldsymbol{x}, t)$ is the velocity vector in Cartesian coordinates as a function of the time t and of the position vector $\boldsymbol{x}$; $\boldsymbol{S} \equiv S_{ij} = \frac{1}{2}(\partial u_i/\partial x_j + \partial u_j/\partial x_i)$ is the deformation rate tensor; p is the pressure, $\boldsymbol{g} = (0, 0, -|g|)$ is the acceleration of gravity vector and $\boldsymbol{\tau}^{\boldsymbol{R}}$ is the Reynolds stress tensor, which is further discussed in Section 3.3.

3.2. Interface-capturing method

Water and mud are treated as immiscible fluids as the interest is on the macro-scale influence of mud on the ship's resistance. Consequently, turbulent mixing that may occur at the mud–water interface is not modelled. This assumption is considered reasonable for three reasons: (i) the absence of propellers, (ii) the damping effects due to the high viscosity of mud, and (iii) the stabilising effect of gravity. The mud–water interface is thus captured using the Volume-Of-Fluid (VOF) method of Hirt and Nichols (1981), which considers a single continuum fluid having density ρ and viscosity μ defined as

$$\rho = \rho_w c + \rho_m (1 - c) \tag{3}$$

$$\mu = \mu_w c + \mu_m (1 - c) \tag{4}$$

where c is the volume fraction whereas the subscripts 'w' and 'm' refer to water ($c = 1$) and mud ($c = 0$), respectively. When the mud layer is modelled as a Newtonian fluid, μ_m is a constant equal to the molecular viscosity of the fluid, whereas when the mud layer is modelled as a Bingham fluid, μ_m is a function of the shear rate (see Section 3.4).

The mud–water interface is assumed to be the locus of points where $c = 0.5$. The use of an alternative expression to Eq. (4) is discussed in Section 6.2.5. The problem is closed by solving a transport equation for c,

$$\frac{Dc}{Dt} \equiv \frac{\partial c}{\partial t} + \boldsymbol{u} \cdot \nabla c = 0 \tag{5}$$

which implies that the volume fraction of a fluid element is conserved and it is transported with the flow.

3.3. Turbulence modelling

The Reynolds stress tensor, $\boldsymbol{\tau}^{\boldsymbol{R}}$, is modelled following the Boussinesq hypothesis:

$$\boldsymbol{\tau}^{\boldsymbol{R}} \equiv \tau_{ij}^R = 2\mu_t S_{ij} - \frac{2}{3}\rho \delta_{ij} k \tag{6}$$

where δ_{ij} is the Kronecker symbol, k is the turbulent kinetic energy (TKE) and μ_t is the so-called eddy (or turbulent) viscosity.

In this work, μ_t is calculated using the SST model of Menter et al. (2003), a standard choice in ship hydromechanics:

$$\mu_t = \frac{\rho a_1 k}{\max(a_1 \omega, \dot{\gamma} F_2)} \tag{7}$$

where ω is the specific dissipation rate of TKE, $\dot{\gamma} = \sqrt{2 S_{ij} S_{ij}}$ is the shear rate. The problem is closed by solving the transport equations for k and ω:

$$\frac{D(\rho k)}{Dt} = \tilde{P}_k + \nabla \cdot \left[(\mu + \sigma_k \mu_t)\nabla k\right] - \rho \beta^* k \omega \tag{8}$$

$$\frac{D(\rho \omega)}{Dt} = \frac{\rho \alpha}{\mu_t}\tilde{P}_k + \nabla \cdot \left[(\mu + \sigma_\omega \mu_t)\nabla \omega\right] - \beta \rho \omega^2 + 2\rho(1 - F_1)\frac{\sigma_{\omega 2}}{\omega}\nabla k \cdot \nabla \omega\,. \tag{9}$$

F_2, F_1, a_1, $\tilde{P}_k$, σ_k, σ_ω, β^*, β, α are given in Appendix A. It is remarked that the SST model is developed for Newtonian fluids, hence its application to non-Newtonian fluids may produce inaccurate results. The discussion about turbulence modelling is deferred to Section 6.2.4. For the interested reader, a more detailed discussion about applications of RANS models for Newtonian fluids to non-Newtonian flows can be found in Lovato et al. (2022a) and Lovato (2023).

3.4. Rheological model for the mud layer

While water is a notorious example of Newtonian fluid, mud exhibits a complex non-Newtonian rheology (see e.g. Coussot, 2017) for a thorough overview on the topic). One important rheological characteristic of mud is the yield stress, i.e. the level of shear stress below which mud behaves as a solid-like material. As the yield stress is exceeded, mud flows as a viscous fluid.

In this work, the yield-stress behaviour of mud is described by the Bingham model (Chhabra and Richardson, 2008; Irgens, 2014), which is the simplest yield-stress model. For the Bingham model, the viscosity reads:

$$\mu_m = \begin{cases} \frac{\tau_B}{\dot{\gamma}} + \mu_B & \text{for} \quad \tau_B \le \tau \\ +\infty \quad (S_{ij} = 0) & \text{for} \quad \tau < \tau_B \end{cases} \tag{10}$$

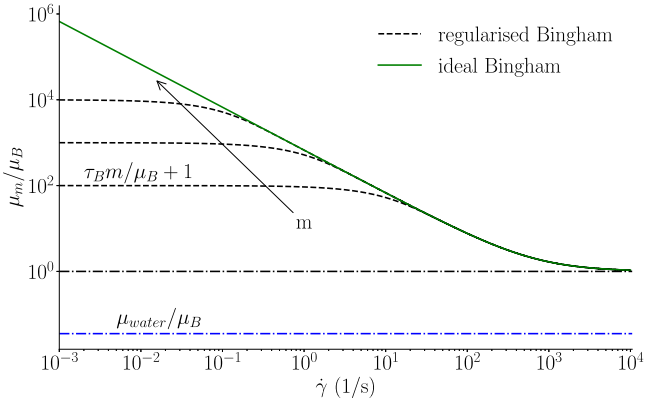

Fig. 4. Effect of the regularisation parameter m on the mud viscosity.

where τ_B (Pa) and μ_B (Pa s) are the Bingham yield stress and viscosity, respectively; $\dot{\gamma}$ is the already defined shear rate; $\tau = \sqrt{\tau_{ij}\tau_{ij}/2}$ is the shear stress calculated as the second invariant of the stress tensor, $\boldsymbol{\tau} \equiv \tau_{ij} = 2\mu_m S_{ij}$.

The infinite viscosity mimics the fact that no deformation occurs ($S_{ij} = 0$) when the shear stress is below the yield stress. However, since an infinite viscosity cannot be numerically handled, Eq. (10) is approximated using the regularisation of Papanastasiou (1987):

$$\mu_m = \frac{\tau_B(1 - e^{-m\dot{\gamma}})}{\dot{\gamma}} + \mu_B\,\dot{\gamma} \tag{11}$$

where m (s) is the regularisation parameter. In the limit of $m \to \infty$, Eq. (11) tends to Eq. (10). The effect of the regularisation on the mud viscosity is illustrated in Fig. 4, which shows that μ_m ranges between $\tau_B m + \mu_B$ and μ_B. Hence, the regularisation parameter controls the maximum viscosity attainable by the fluid. The non-dimensional regularisation parameter, M, is here defined as the ratio of maximum-to-minimum viscosity:

$$M = \frac{\tau_B m}{\mu_B} + 1 \simeq \frac{\tau_B m}{\mu_B}\,. \tag{12}$$

If one wants to simulate an ideal Bingham fluid as closely as possible, a very large M shall be used. However, difficult convergence of the iterative solver often arises before such independence is reached (Syrakos et al., 2013; Lovato et al., 2022c). On the other hand, previous research (e.g. Dzuy and Boger, 1985; Ellwood et al., 1990) suggested that regularised models could better describe the flow behaviour of real fluids, which in fact do not exhibit an infinite viscosity. In this work, $M = 16000$ is used for all calculations unless stated otherwise. Such value is deemed sufficient to capture the yield-stress (viscoplastic) behaviour of mud while ensuring good convergence of the iterative solver. The influence of the regularisation parameter on the resistance is discussed in Section 6.2.3.

3.5. Resistance calculation

This study focuses on the ship's resistance. The total ship's resistance coefficient, R_T, is calculated as the sum of the frictional and pressure components as:

$$R_T = R_P + R_F \tag{13}$$

$$R_F = \int_S \Big(\boldsymbol{\tau}\cdot\boldsymbol{n}\Big)_x dS\,, \qquad R_P = \int_S \Big(-p\boldsymbol{n}\Big)_x dS \tag{14}$$

where S is the wetted hull surface, $\boldsymbol{n}$ is its outward normal vector and the subscript x indicates the x-component of a vector. The computed forces are reported in non-dimensional form as:

$$C_T = C_F + C_P \equiv \frac{|R_F| + |R_P|}{\frac{1}{2}\rho_w S V^2}\,. \tag{15}$$

Table 2
Fluid properties of sea water (standard conditions), three non-Newtonian mud conditions and a 'Newtonian version' of Mud_23.

Fluid	ρ (kg/m^3)	τ_B (Pa)	μ_B (Pa s)
Sea water	1026	–	0.00122
Mud_10	1171	9.96	0.0172
Mud_17	1190	17.3	0.0249
Mud_23	1200	23.0	0.0344
Mud_23Nwt	1200	0.0	0.0344

4. Simulated test cases

4.1. Properties of water and mud

In order to consider somewhat realistic mud properties, the three mud conditions that were used in our previous work (Lovato et al., 2022b) are selected. These three mud conditions are respectively labelled as Mud_10, 17, and 23, and their properties are summarised in Table 2. An additional fictitious condition is simulated by setting the yield stress of Mud_23 to zero. This 'Newtonian version' will be identified as Mud_23Nwt and it will serve the purpose of illustrating the effect of neglecting the mud yield stress.

4.2. Densimetric froude number

An important parameter for stratified flows is the densimetric Froude number, i.e. the ratio of the flow speed to the critical speed of the internal waves:

$$Fr_i = \frac{V}{V_{crit}} \tag{16}$$

where the subscript i refers to the internal wave. Various definitions of V_{crit} are used in the literature. For example, Miloh et al. (1993) demonstrated that a peak in the resistance occurs at the following critical speed:

$$V_{crit}^2 = g(1-\gamma)\frac{h_w h_m}{h_m\gamma + h_w} \tag{17}$$

with $\gamma = \rho_w/\rho_m < 1$. Other definitions used e.g. in Sellmeijer and van Oortmerssen (1984) and Esmaeilpour et al. (2018) can be obtained from Eq. (17) in the limit of a thin lower layer ($h_m \to 0$) or a thin upper layer ($h_w \to 0$), respectively.

On the other hand, Sano and Kunitake (2018) used the definition of critical Froude number derived by Yeung and Nguyen (1999), which can be rearranged in terms of critical speed as:

$$V_{crit}^2 = gh\Big[\frac{1}{2} - \sqrt{\frac{1}{4} - (1-\gamma)\frac{h_w h_m}{h^2}}\Big] \tag{18}$$

with $h = h_m + h_w$. Eqs. (17) and (18) differ from each other for small γ and h_w/h_m. However, it can be shown that for realistic bottom conditions of practical interest, the difference between the two expressions does not exceed 2%–3%. In this work, Fr_i is defined using Eq. (17) because of its simpler expression.

4.3. Flow conditions

The simulations are carried out for sailing speeds between about 3 and 9 knots, a realistic range for navigation in confined areas. Table 3 shows the corresponding densimetric Froude number (reported for Mud_23 and UKC = 0), which ranges from sub-critical ($Fr_i < 1$) to super-critical ($Fr_i > 1$). The under-keel clearance is varied from +20 to −20% of the ship's draught.

The other reported non-dimensional parameters are the Reynolds number, $Re = \rho_w V L/\mu_w$, the Froude number, $Fr = V/\sqrt{gL}$, and the depth-Froude number, $Fr_h = V/\sqrt{gh}$. Both Fr and Fr_h are small enough to justify the frictionless rigid lid (or double-body) approach for the air–water free surface.

Table 3
Simulated flow conditions. The densimetric Froude number, Fr_i, is given for UKC = 0 and Mud_23 ($\rho_w/\rho_m \equiv \gamma = 0.855$).

V (m/s)	V (knots)	Fr_i	Re	Fr	Fr_h
1.50	2.92	0.47	4.04×10^8	0.027	0.09
2.00	3.89	0.62	5.38×10^8	0.036	0.11
2.25	4.37	0.70	6.06×10^8	0.040	0.13
2.50	4.86	0.78	6.73×10^8	0.045	0.14
2.75	5.35	0.85	7.40×10^8	0.049	0.16
3.00	5.83	0.93	8.07×10^8	0.054	0.17
3.25	6.32	1.01	8.75×10^8	0.058	0.19
3.50	6.80	1.09	9.42×10^8	0.062	0.20
4.00	7.78	1.24	1.08×10^9	0.071	0.23
4.50	8.75	1.40	1.21×10^9	0.080	0.26

5. Computational setup

5.1. Flow solver

The CFD code used for this work is ReFRESCO (Vaz et al., 2009), a viscous-flow code currently being developed and verified for maritime purposes by the Maritime Research Institute of the Netherlands (MARIN) in collaboration with several non-profit organisations around the world. Originally developed for Newtonian fluids, ReFRESCO has been recently extended and verified for flow simulations of Herschel–Bulkley fluids (Lovato et al., 2021, 2022c,a; Lovato, 2023), of which Bingham is a particular case.

Equations are discretised in strong-conservation form with a second-order finite-volume method for unstructured meshes with cell-centred co-located variables. Mass conservation is ensured with a pressure-correction equation based on a SIMPLE-like algorithm (Klaij and Vuik, 2013). The advective fluxes of the volume-fraction equation are discretised with an interface-capturing scheme (Klaij et al., 2018), which blends compressive and high-resolution interpolation schemes. The advective fluxes of the other transport equations are discretised with the Harmonic scheme (van Leer, 1979). The non-linear advection term in the momentum equation is linearised with the Picard method.

5.2. Grids

Because of the symmetry of the problem, only half domain is modelled to save computational time. The half-domain is discretised with a series of unstructured hexahedral grids, which are 10L long (5 astern and 4 ahead of the ship) and 6L wide. The bottom boundary is located at a depth corresponding to $h/T = 1.5$, whereas the top boundary is at the undisturbed water level.

The grids are gradually refined near the ship using concentric boxes to capture more details of the flow field around the ship (Fig. 5(a)). The bottom of the domain is also refined, but only within a radius of about 2L from the ship. On the hull, a higher refinement level is applied to the aft and fore body and near the stern tube (Fig. 5(c, d)). Anisotropic refinement is applied around the hull to capture the boundary layer development (Fig. 5(f)). This refinement region is also known as 'inflation' or 'prism' layer.

Five grids, labelled as G5, G4, G3, G2 and G1, are generated for the grid-sensitivity study. The grids are obtained using the method of Crepier (2017) to preserve the geometrical similarity of unstructured grids as much as possible. Two refinements ratios are considered: (i) $r_i^V = \sqrt[3]{N_c^V(\mathrm{G1})/N_c^V(\mathrm{Gi})}$, where $N_c^V(\mathrm{Gi})$ is the total number of cells for the ith grid; (ii) $r_i^S = \sqrt[2]{N_c^S(\mathrm{G1})/N_c^S(\mathrm{Gi})}$, where $N_c^S(\mathrm{Gi})$ is the number of cell faces on the hull for the ith grid.

For truly geometrically similar grids, $r_i^V = r_i^S$. Table 4 shows that the two refinement ratios are almost identical, which indicates a good geometrical similarity between the five unstructured grids. An impression of the difference between G1 and G4 is shown in Fig. 5(b), whereas the main parameters of the five grids are reported in Table 4.

Table 4
Number of grid cells in the half-ship domain (N_c^V) and on the (half) hull (N_c^S), and corresponding refinement ratios r_i^V and r_i^S; y_{avg}^+ and y_{max}^+ are the average and maximum y^+ on the first cell away from the hull at $Re = 1.21 \times 10^9$ ($V = 4.5$ m/s) without mud.

Grid label	N_c^V	r_i^V	N_c^S	r_i^S	y_{avg}^+	y_{max}^+
G1 (very fine)	52,381,409	1.00	242,615	1.00	0.16	0.25
G2 (fine)	30,963,350	1.19	169,408	1.20	0.19	0.30
G3 (medium)	15,958,776	1.49	108,459	1.50	0.24	0.37
G4 (coarse)	6,799,173	1.98	61,079	1.99	0.33	0.49
G5 (very coarse)	2,054,964	2.94	27,546	2.97	0.52	0.78

Calculations without mud are performed on the finest grid, G1. Table 4 also shows that for the case with the highest Reynolds number ($V = 4.5$ m/s), the maximum $y^+ = \rho u_\tau d/\mu$ (d is the distance between the centroid of the first cell away from the wall and the wall boundary and $u_\tau = \sqrt{\tau_w/\rho}$, with τ_w being the wall shear stress) on G1 does not exceed 0.25, which is an acceptable resolution for wall-resolved simulations with the SST model (Eça et al., 2018).

For the calculations with mud, G4 is used as initial grid while Adaptive Mesh Refinement (AMR) (Windt, 2013) is applied around the mud–water interface. An example of simulation with mud on G4 after applying AMR is illustrated in Fig. 5(e). The grid sensitivity of the ship's resistance is discussed in Section 6.1.

5.3. Boundary conditions

5.3.1. Inlet

A uniform velocity $\boldsymbol{u} = (-V, 0, 0)$ is imposed at the inlet boundary, whereas Neumann conditions are applied for pressure. Dirichlet conditions are applied for k and ω as follows:

$$k = \frac{3}{2}(UI)^2, \quad \omega = \frac{\rho k}{\mu_t} \tag{19}$$

where I is the turbulence intensity. The inlet conditions are completed by setting I and μ_t; in this work, we adopted $I = 0.01$ and $\mu_t/\mu \simeq 10$, a typical choice for full-scale simulations. For simulations with mud, the inlet turbulent viscosity reads:

$$\mu_t = \begin{cases} 10\mu_w & \text{for} \quad c = 1 \quad \text{(water)} \\ 10\mu_B & \text{for} \quad c = 0 \quad \text{(mud)} \end{cases} \tag{20}$$

Note that other values for I and μ_t were also tested but no meaningful change was observed. Finally, Dirichlet conditions are applied for the volume fraction.

5.3.2. Ship

Impermeable/no-slip boundary conditions are applied for the velocity ($\boldsymbol{u} = 0$), whereas the Neumann condition is set for pressure ($\partial p/\partial n = 0$) and volume fraction. For the turbulence quantities, $k = 0$ whereas for ω the following value is imposed at the first cell-centre away from the wall:

$$\omega = \frac{80\mu}{\rho d^2} \tag{21}$$

where d is the distance from the wall. The value of ω at the hull surface is set to 10 times the value given by Eq. (21), as described by Menter (1994).

5.3.3. Top and side planes

The top and side planes are regarded as symmetry planes, i.e. the normal velocity component is set to zero ($\boldsymbol{u} \cdot \boldsymbol{n} = 0$) while Neumann conditions are applied for all other scalar fields ($\nabla\phi \cdot \boldsymbol{n} = 0$).

5.3.4. Bottom

In order to be consistent with the forward motion of the ship, the inflow velocity is imposed on the bottom ($\boldsymbol{u} = (-V, 0, 0)$) while Neumann conditions are applied for pressure and volume fraction. Fur-

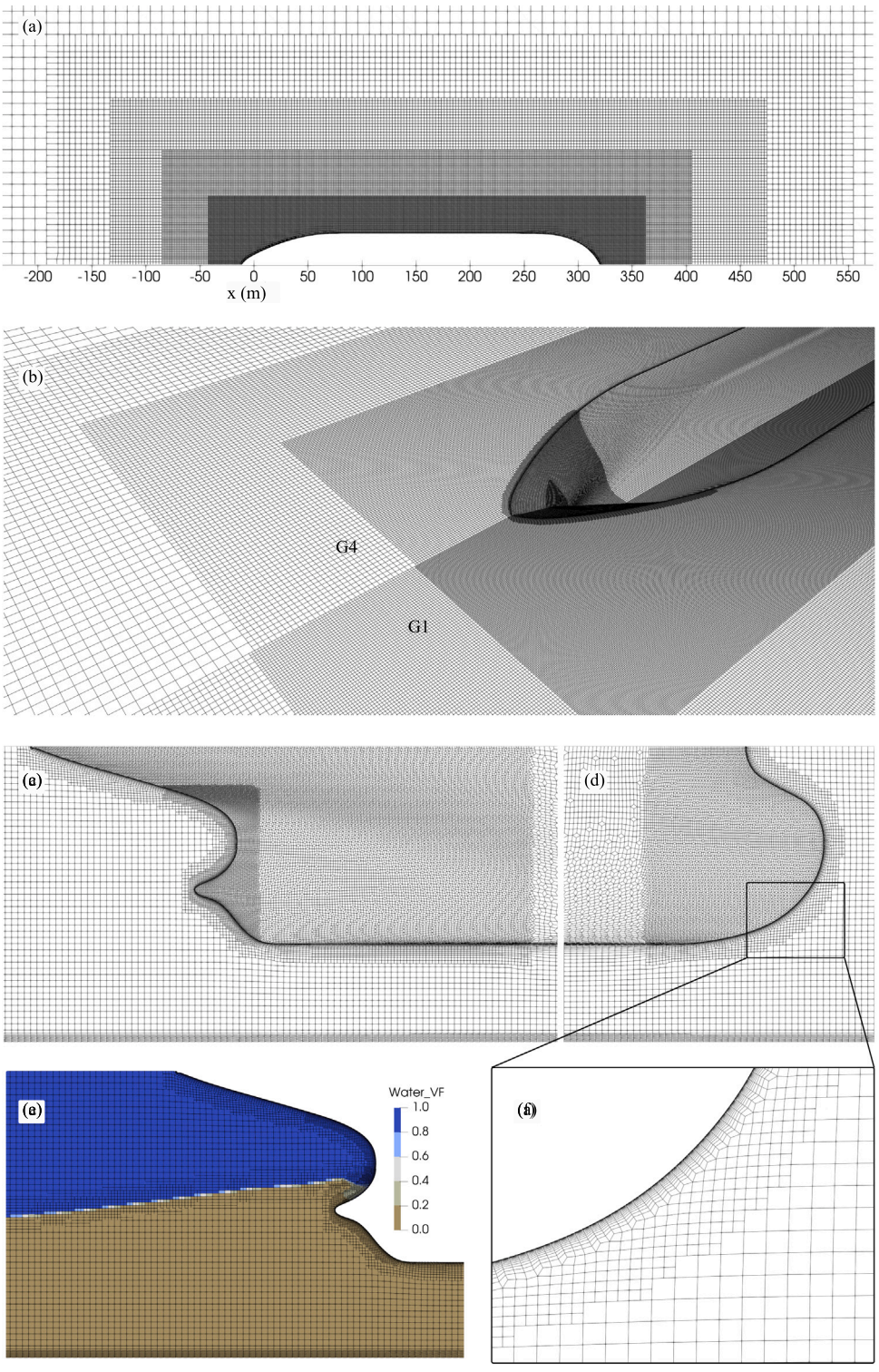

Fig. 5. Illustrations of the grid topology: (a) top boundary of G4; (b) comparison of coarsest (G4) and finest grid (G1); (c, d) symmetry plane of G4 near the aft and fore body of KVLCC2; (e) example of G4 after applying adaptive mesh refinement around the mud–water interface; (f) enlargement of the near-wall mesh (prism layer).

thermore, to avoid excessive mesh refinement in the bottom region, the so-called "automatic" wall functions are applied, which blend between the known near-wall behaviour in the viscous sub-layer and the log-layer. In practice, the eddy-viscosity on the bottom wall is expressed as:

$$\mu_t = \mu\left(\frac{y^+}{u^+} - 1\right) \tag{22}$$

where

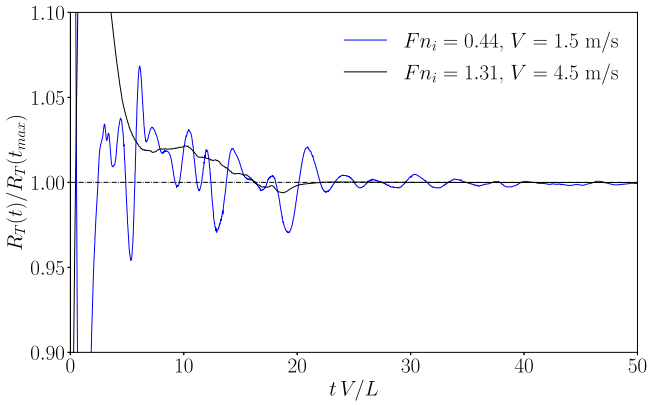

Fig. 6. Convergence history of the total resistance at the lowest (subcritical) and highest (supercritical) speed with UKC = −20%.

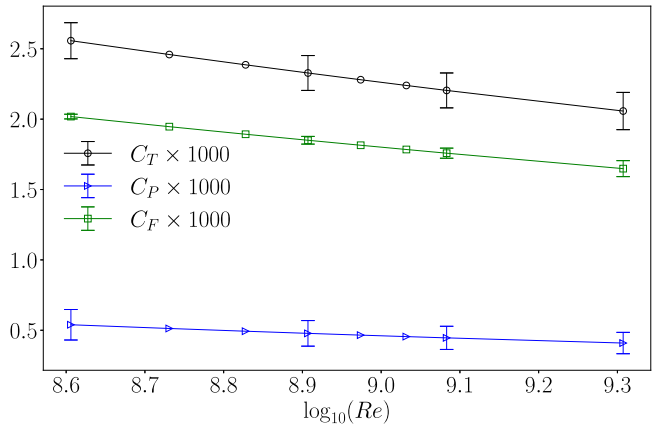

Fig. 7. Resistance coefficients of KVLCC2 calculated on the finest grid (G1) when sailing above solid bottoms (no mud) with $h/T = 1.5$.

$$u^+ \equiv \frac{u}{u_\tau} = \left[\left(\frac{1}{y^+}\right)^4 + \left(\frac{\kappa}{\ln(y_*^+ E)}\right)^4\right]^{-0.25} \tag{23}$$

with $E = 8.43$, $\kappa = 0.41$ and $y_*^+ = \max(y^+, 1/E)$, which excludes the negative part of the logarithm. Note that for simulations with mud, y^+ is calculated using the viscosity from Eq. (4). For the turbulent quantities:

$$k = 0 \tag{24}$$

$$\omega^+ \equiv \frac{\omega\mu}{\rho u_\tau^2} = \left[\left(\frac{80}{(y^+)^2}\right)^2 + \left(\frac{1}{\kappa\sqrt{C_\mu}(y^+)}\right)^2\right]^{0.5} \tag{25}$$

with $C_\mu = 0.09$. As for Eq. (21), Eq. (25) is applied on the first cell centre away from the boundary.

5.3.5. Outlet

Dirichlet conditions are applied for pressure using the hydrostatic pressure, whereas Neumann conditions are applied for all the other quantities.

5.4. Unsteady simulations settings

All simulations are run in unsteady mode although the interest is in the steady solution. For the calculations without mud, the solution did not show any unsteadiness, and results were virtually indistinguishable from the results obtained with steady calculations.

For the case with mud, all simulations were run in unsteady mode. An initial wave damping zone was applied in the far field in order to mitigate start-up effects. The wave damping zone was only active at the initial part of the simulations. The non-dimensional time step, $\Delta tV/L$, was set between 0.02 and 0.14, depending on the densimetric Froude number. Sub-critical simulations showed much stronger unsteadiness than super-critical simulations (Fig. 6), hence smaller time steps were needed for subcritical calculations ($Fr_i < 1$). In general, statistically steady solutions were achieved after a total simulated non-dimensional time, $t_{tot}V/L$, between 60 and 280, depending on the test case.

The computed forces are the average value over the last 500 time steps. The standard deviations were on average below 0.1% of the mean value and they never exceeded 0.5%. The statistical uncertainties are therefore neglected.

6. Results and discussion

6.1. Numerical errors and uncertainties

Before discussing the effect of mud on the ship's resistance, it is important to assess the influence of numerical errors. For statistically steady flows, numerical errors are commonly divided into three components: round-off, iterative and discretisation errors. Since the present calculations are performed on a double-precision machine, round-off errors can be safely neglected. Iterative errors stem from the use of iterative methods to find the solution of the discretised equations. The iterative uncertainties (estimated with the method of Eça and Hoekstra, 2009) were found to be about two orders of magnitude lower than the discretisation uncertainties, hence they are not further discussed. In the remainder, only the discretisation uncertainties are discussed. Firstly, the numerical uncertainties associated with calculations with only water are presented. Subsequently, the uncertainties for a ship sailing above a Newtonian mud layer (referred to as Mud_23Nwt) are investigated.

Table 5
Discretisation uncertainties in percentage of the corresponding resistance coefficient component for the lowest, intermediate and highest speed when sailing above solid bottoms (no mud) with $h/T = 1.5$.

Grid	r_i^S	$C_F \times 10^3$	U_{C_F}(%)	$C_P \times 10^3$	U_{C_P}(%)	$C_T \times 10^3$	U_{C_T}(%)
$Re = 4.04 \times 10^8$ ($V = 1.5$ m/s)							
G1	1.00	2.018	0.8	0.539	20.1	2.557	5.0
G2	1.20	2.014	1.1	0.526	23.6	2.540	5.9
G3	1.50	2.005	1.7	0.516	26.6	2.521	6.9
G4	1.99	1.987	2.8	0.506	29.5	2.493	8.4
$Re = 8.07 \times 10^8$ ($V = 3.0$ m/s)							
G1	1.00	1.850	1.5	0.478	19.0	2.328	5.3
G2	1.20	1.844	1.9	0.467	22.3	2.311	6.3
G3	1.50	1.833	2.7	0.459	25.0	2.292	7.4
G4	1.99	1.813	4.1	0.451	27.7	2.264	9.0
$Re = 1.21 \times 10^9$ ($V = 4.5$ m/s)							
G1	1.00	1.758	2.0	0.446	18.5	2.204	5.6
G2	1.20	1.751	2.6	0.436	21.7	2.187	6.7
G3	1.50	1.739	3.5	0.429	24.2	2.167	7.9
G4	1.99	1.717	5.1	0.422	26.7	2.139	9.6

6.1.1. Solid bottoms (no mud)

The discretisation uncertainties, U, were estimated with the method of Eça and Hoekstra (2014) using four of the five grids presented in Section 5.2. The discretisation uncertainties are reported in Table 5 for the lowest, intermediate and highest speed. The resistance coefficients calculated on G1 are plotted in Fig. 7 for the entire speed range. Additionally, an extra speed of 7.54 m/s ($Re = 2.03 \times 10^9$) is included, which is used later in this section for comparison with literature data.

As expected, U_{C_F} decreases with grid refinement and increases with Re (higher Re implies larger velocity gradients at the wall). On the other hand, U_{C_P} remains quite large even on the finest grid ($U_{C_P} \approx$ 20%). This is attributed to the fact that C_P stems from the difference

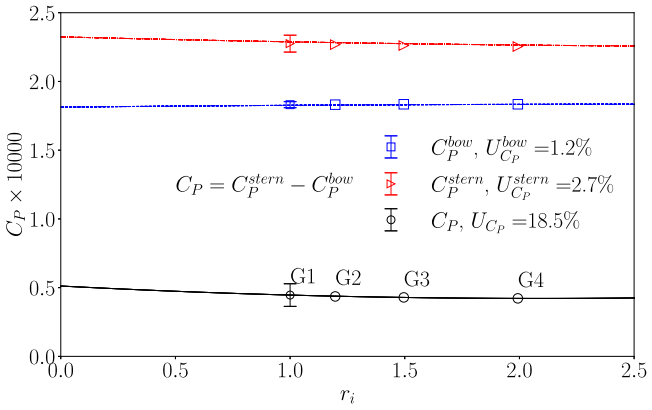

Fig. 8. Grid sensitivity of the bow and stern (hydrodynamic) contributions of C_P when sailing at $V = 4.5$ m/s ($Re = 1.21 \times 10^9$) above solid bottoms (no mud) with $h/T = 1.5$.

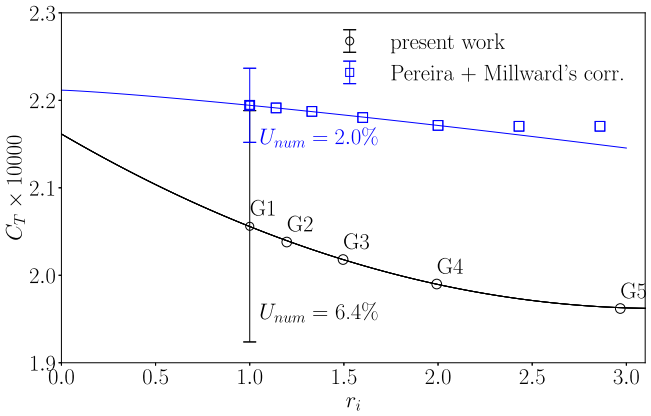

Fig. 9. Grid sensitivity of C_T for $V = 7.54$ m/s ($Re = 2.03 \times 10^9$, $Fn = 0.135$) and comparison with C_T of Pereira et al. (2017) corrected for $h/T = 1.5$ using the Millward's formula.

between two large pressure contributions, from the stern and the bow. Fig. 8 shows that the grid sensitivity of the stern and bow component is rather small. However, the discretisation uncertainty associated with the difference between these components increases by one order of magnitude. In any case, U_{C_P} is still small compared to the effect of mud (which is discussed in Section 6.3), hence they are deemed acceptable for the purpose of this work.

As already mentioned, additional calculations were carried out at $Re = 2.03 \times 10^9$ for comparison with the previous results of Pereira et al. (2017). Their deep-water total resistance coefficient, C_T^{dw}, has been corrected for shallow water ($h/T = 1.5$) as:

$$C_T^{sw} = \left(\frac{C_T^{dw}}{C_{F_0}} + \Delta k \right) \cdot C_{F_0} \tag{26}$$

where $\Delta k = 0.644(T/h)^{1.72}$ is the Millward's formula (Millward, 1989) to correct the form factor for shallow water conditions (see e.g. Toxopeus, 2013; Zeng et al., 2019). The plate friction coefficient, C_{F_0}, is calculated using the ITTC'57 friction line as $C_{F_0} = 0.075/(\log_{10}(Re)-2)^2$. The comparison is shown in Fig. 9 for different refinement levels. Note that the numerical uncertainty of Pereira et al. (2017) is for deep-water calculations, hence the actual uncertainty for shallow water would most likely have been larger. In any case, the uncertainty bars in Fig. 9 overlap, hence the difference in C_T is mostly attributed to numerical errors and to the Millward's correction. The trends in Fig. 9 also suggest that the discrepancy would reduce with further grid refinement.

In conclusion, present results agrees well with Pereira et al. (2017), and the numerical uncertainties in C_F, C_P and C_T are deemed acceptable for the purpose of this work.

6.1.2. Muddy bottoms

Calculations with muddy bottoms are far more computationally expensive than with solid bottoms because of the:

- additional VOF equation for the mud–water interface;
- extra refinement around the mud–water interface;
- transient effects associated with the internal wave, requiring more time steps to obtain a statistically steady solution;
- large number of test cases due to the additional parameters related to the mud layer (e.g. UKC, mud density and thickness);
- additional quantities such as the shear rate and the mud viscosity that need to be computed at each outer iteration when simulating Bingham fluids;
- flow-dependent viscosity of mud which makes the convergence of the iterative solver more difficult, often requiring more iterations or to restart the simulation from a 'Newtonian' test case.

Table 6
Discretisation uncertainties in percentage of the corresponding resistance coefficient component for the lowest, intermediate and highest speed when sailing above muddy bottoms (Mud_23Nwt, UKC = +20%) with $h/T = 1.5$. r_i^V is based on the total number of cells after applying adaptive mesh refinement at the mud–water interface.

Grid	r_i^V	$C_F \times 10^3$	U_{C_F}(%)	$C_P \times 10^3$	U_{C_P}(%)	$C_T \times 10^3$	U_{C_T}(%)
$Re = 4.04 \times 10^8$ ($V = 1.5$ m/s, $Fr_i = 0.55$)							
G1	1.00	2.159	1.6	2.099	1.6	4.258	1.5
G2	1.18	2.155	2.1	2.093	2.3	4.247	2.2
G3	1.46	2.143	2.7	2.061	4.7	4.204	4.0
G4	1.94	2.122	3.9	1.854	18.4	3.976	11.8
G5	2.75	2.080	6.5	2.013	14.3	4.093	13.6
$Re = 8.07 \times 10^8$ ($V = 3.0$ m/s, $Fr_i = 1.11$)							
G1	1.00	1.866	1.6	19.88	11.5	21.74	10.3
G2	1.18	1.859	2.1	20.33	12.9	22.19	11.6
G3	1.46	1.846	3.0	20.70	14.9	22.55	13.4
G4	1.94	1.827	4.3	21.01	17.7	22.84	15.9
G5	2.75	1.781	7.6	21.79	20.6	23.57	18.4
$Re = 1.21 \times 10^9$ ($V = 4.5$ m/s, $Fr_i = 1.66$)							
G1	1.00	1.811	2.4	7.860	8.8	9.670	5.4
G2	1.18	1.801	2.9	7.790	8.9	9.591	5.5
G3	1.46	1.789	3.8	7.825	8.8	9.615	5.5
G4	1.94	1.770	5.3	7.997	8.6	9.766	5.4
G5	2.75	1.725	8.6	8.019	8.6	9.744	5.4

To keep the computational costs reasonable, the grid refinement is done only with Mud_23Nwt and the UKC = +20% (percentage of T) for the lowest, intermediate and highest speed. The estimated discretisation uncertainties are given in Table 6 together with the resistance coefficients. Note that because AMR is applied, the uncertainty estimation is now performed using the volume-based refinement ratio, r_i^V.

Compared to the case with solid bottoms, U_{C_F} is slightly larger but it exhibits the expected behaviour: it decreases with grid refinement and it increases with Re. Furthermore, C_F converges monotonically with grid refinement, contrary to C_P. This is particularly evident at the lowest speed, where U_{C_P} is rather large for G4 and G5. The reason for this is ascribed to the hydrostatic component of C_P, which is calculated as:

$$C_P^{hs} = \frac{1}{\frac{1}{2}\rho_w S V^2} \int_S \left[\rho_w g (z - T) \boldsymbol{n} \right]_x dS \,. \tag{27}$$

where $\boldsymbol{n}$ is the outward normal vector of the hull. If no contact with mud occurs, as in this case, C_P^{hs} must be zero (or, in any case, close to machine precision) because of the double-body assumption for the air–water interface. However, the discretisation of the hull can cause an imbalance between the large contributions of the bow and the stern.

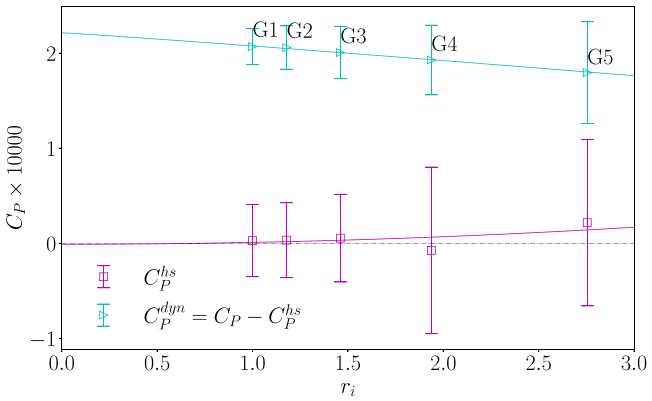

Fig. 10. Grid sensitivity of the hydrostatic and dynamic part of C_P when sailing at 1.5 m/s (Mud_23Nwt, UKC = +20%).

In fact, as the hull is divided into quadrilateral cells faces, there is no guarantee that the four vertices are coplanar, especially in regions with high curvature such as at the fore and aft ends of the ship. Since the cell faces are assumed to be planar when calculating the face area and the normal vector, some errors are introduced. Although these errors are typically rather small, when integrated over the hull they may result in a noticeable imbalance between the bow and stern contributions, resulting in a small but non-zero contribution of the hydrostatic pressure to the resistance.

Fig. 10 shows that C_P^{hs} at the lowest speed is not zero, although it does tend to zero with refinement. Its convergence is oscillatory, contrary to the dynamic component, C_P^{dyn}, confirming that the oscillatory behaviour of C_P is caused by the hydrostatic component. Analogous trends of C_P^{hs} were found at the higher speeds, but this had virtually no influence on the estimation of U_{C_P} because of the much larger dynamic component.

Unless stated otherwise, further calculations with mud are performed on G4 as a trade-off between computational costs and accuracy.

6.2. Numerical effects on the resistance

6.2.1. Numerical ventilation (NV)

When sailing through mud, i.e. with negative UKC, the frictional resistance is expected to increase because of contact with mud. However, there are two effects that can significantly reduce the contact area between the hull and the mud layer.

The first effect is purely numerical and it is often referred as "numerical ventilation" (NV) in the literature. This effect typically consists in the air volume-fraction being convected in the boundary layer below the water line, causing a reduction of the skin friction. NV is commonly encountered when modelling planing hulls using the VOF method (Gray-Stephens et al., 2021; Avci and Barlas, 2018; Viola et al., 2012), where the hull forms a small acute angle with the free surface. As the latter has the tendency to align with the thin cells close to the hull, air is convected into the water. Of course, in this work, the interface is between water and mud instead of air and water.

Although NV does not typically occur for displacement hulls, the problem investigated in this work is an exception. In fact, with small negative UKC, the mud–water interface forms a small acute angle with the bulbous bow. Fig. 11 confirms indeed that NV does not occur with UKC = −40%, wheres it occurs for UKC = −20% and −10%. This also means that, because UKC = −20% and −10% are more realistic than UKC = −40%, NV will likely occur in practical simulations.

While it is not possible to completely eliminate NV, there are some strategies to reduce it (Gray-Stephens et al., 2021). One consists in artificially "extracting water" within a small distance from the hull, as

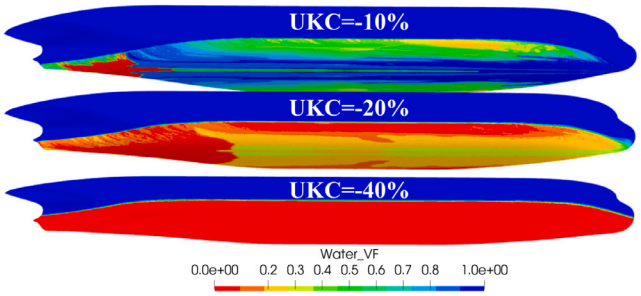

Fig. 11. Effect of numerical ventilation on the volume-fraction when sailing through mud. The ship is sailing at 1.5 m/s through Mud_23Nwt.

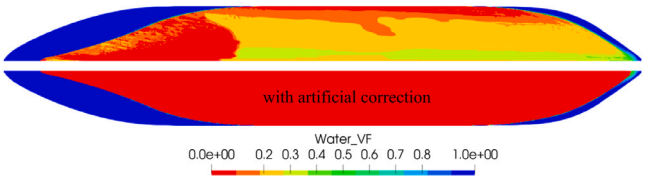

Fig. 12. Water volume-fraction without (top) and with (bottom) the artificial correction to suppress NV. The ship is sailing with UKC = −20% at 1.5 m/s through Mud_23Nwt.

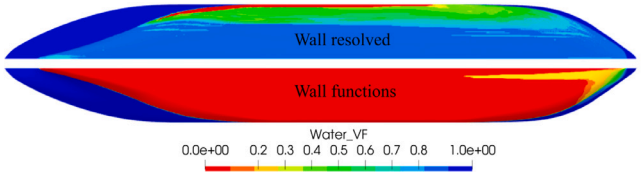

Fig. 13. Water volume-fraction using: (top) wall-resolved grid; (bottom) coarser near-wall mesh combined with wall functions. The artificial correction to reduce numerical ventilation is active for both cases. The ship is sailing with UKC = −20% at $V = 2.5$ m/s through Mud_23Nwt.

suggested by Viola et al. (2012). This is achieved by adding a source term proportional to c in Eq. (5). In this way, the source term will automatically vanish as the water is extracted from the mud layer and the original equation is restored. To minimise mass imbalance, the term is only active in the first few cells close to the hull and, in any case, only when $c < 0.3$. With this method, numerical ventilation was significantly reduced at low speed, as shown in Fig. 12. However, as the speed increases, the interface deforms more and the angle with the bulbous bow reduces, thereby causing more ventilation. In this case, the artificial suppression to reduce NV was found to be insufficient.

Another effective strategy to reduce NV is to increase the cells' height near the hull (Gray-Stephens et al., 2021). This can be done without causing an excessive increase in the discretisation errors by using a coarser near-wall grid in combination with wall functions instead of the wall-resolved approach. This strategy was found to be very effective in reducing NV (Fig. 13). For this reason, further calculations with negative UKC are carried out using wall functions, unless stated otherwise. The use of wall functions is discussed in more detail in Section 6.2.4.

6.2.2. Water lubrication (WL)

The second effect that reduces the contact area between the hull and the mud layer is partly physical and partly numerical, and it is due to the deformation of the mud–water interface above certain speeds. This will be concisely labelled as "water lubrication" (WL).

When sailing at low speed, the mud–water interface barely deforms, even with negative UKC. Hence, numerical ventilation aside, the ship sails through mud as expected (Fig. 14, left). As the speed increases,

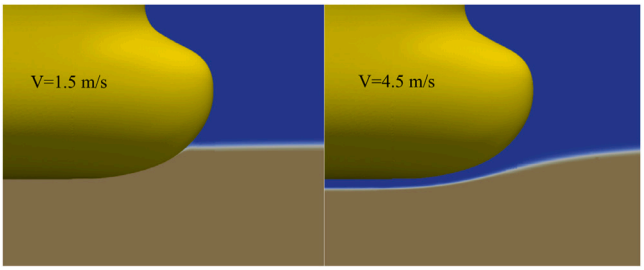

Fig. 14. Mud–water interface at the bow when sailing at the lowest (left) and highest speed (right) with an initial UKC of −20% (percentage of T).

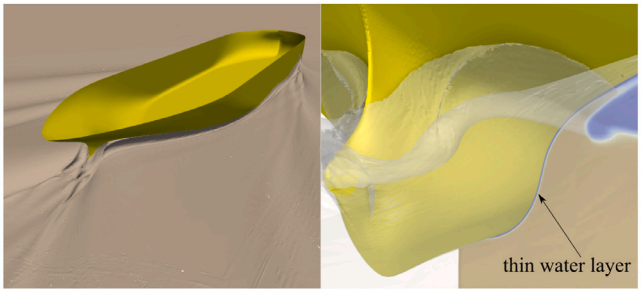

Fig. 15. Bird-view (left) and fish-view (right) of the stern of the ship sailing at $V = 4.5$ m/s with UKC = −20%. The right picture shows the mud–water interface on the cross section at $x/L = 0.1$.

however, so does the pressure at the bow ($\sim V^2$), which becomes strong enough to deform the mud–water interface (Fig. 14, right). This allows water to flow underneath the hull, thereby reducing the contact area with mud. Water lubrication has been observed in the previous numerical studies of Kaidi et al. (2020) (Fig. 23 therein) and Leijs (2021) (Fig. 6.16 therein), although it was not explicitly labelled as such.

While WL starts at the bow as a physically consistent phenomenon, it is probably amplified further downstream by the VOF method because of the assumption of immiscible fluids. In fact, although at 4.5 m/s the ship appears to be in contact with mud (Fig. 15, left), a closer look reveals that a thin water layer still exists all the way down to the stern of the ship (Fig. 15, right). Hence, at such speed, virtually no contact with mud seems to occur, even with UKC = −20%.

Whether such a thin water layer would 'survive' down to the stern is rather questionable. Since the water layer thickness is comparable with the boundary layer thickness ($\sim$ 0.4 m at amidship), turbulence mixing would likely form a mixture of water and mud, having in-between density and viscosity. This, however, cannot be captured by the VOF method and alternative multi-phase approaches for mixtures of water and fine sediments would be required (e.g. Goeree et al., 2016; Ouda and Toorman, 2019). To summarise, WL starts at the bow as a physically consistent phenomenon, whereas it appears to turn into a modelling limitation further downstream.

It is remarked that there is not a sharp distinction between WL and NV since both introduce water in the boundary layer below the initial mud level. However, it is reasonable to classify as WL when $c \approx 1$, i.e. when the hull is in contact with (nearly) only water. On the other hand, when $0.1 \leq c \leq 0.9$, the hull is in contact with a mixture of water and mud, which is a result of NV. Hence, as the speed increases, more and more water is convected in the boundary layer and NV turns into WL, with some NV still occurring on the stern tube (Fig. 16).

In conclusion, both WL and NV tend to reduce the frictional resistance by reducing the contact area with mud when sailing with negative UKC. At high speeds, WL leads to almost no contact with mud, which is considered, at least in part, physically consistent with the deformation

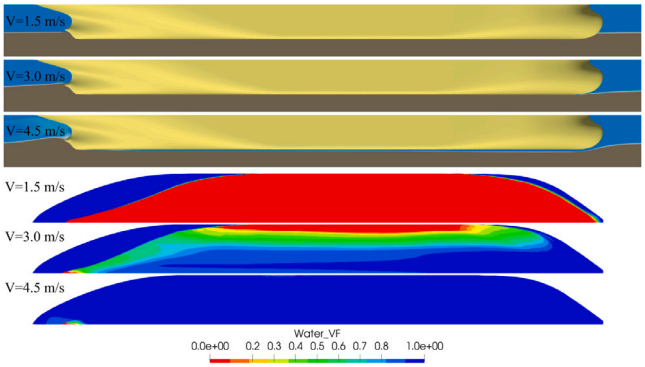

Fig. 16. Water volume fraction on the hull at low, intermediate and high speed. The ship is sailing through Mud_23 with UKC = −20%. Calculations are carried with the artificial suppression of NV and with the wall function approach.

of the interface. At lower speeds, NV becomes dominant but it can be mitigated by using an artificial correction and a coarser near-wall mesh combined with wall functions.

6.2.3. Regularisation parameter

The use of the regularised version of the Bingham model avoids the infinite viscosity for zero shear rate while introducing an arbitrary parameter. In principle, M (see Eq. (12)) must be very large in order to mimic the ideal Bingham model as closely as possible. Large values of M, however, can cause poor convergence of the iterative solver, hence a balance between accuracy and solver's stability must be found. One approach is to gradually increase M until the resistance becomes independent of M. However, this approach can become computationally expensive as several calculations need to be performed (at least one for each value of M). Furthermore, difficult iterative convergence may arise before M-independent solutions are obtained.

Here, the sensitivity of the resistance to M has been investigated for the lowest and highest speed when sailing through Mud_23 with UKC = −20%. The value of M was systematically doubled, starting at 2000 and ending at 256000. The variation of the resistance coefficients for UKC = −20% is shown in Fig. 17, where M increases from right to left.

The resistance coefficients do not seem to be reaching an asymptotic convergence, which suggests that even larger M would be required to reach M-independent results. However, larger M led to poor iterative convergence, making the solution unreliable. Furthermore, increasing M implies larger viscosity gradients and therefore larger discretisation errors.

Nevertheless, Fig. 17 is instructive as it shows that the regularisation parameter is more important at low speeds, especially for C_P, which does not even converge monotonically. Notably, C_P with $M = 2000$ is almost the same as $M = 256000$. At the highest speed (Fig. 17, bottom), on the other hand, a rather small sensitivity is observed. Even with a Newtonian mud, the forces coefficients are just 10% lower than with $M = 256000$. It may be argued that this lower sensitivity is due to the lack of contact with the mud layer because of water lubrication (see Section 6.2.2). However, calculations were also performed with positive UKC and results were surprisingly similar to those in Fig. 17, even at low speed, with the only difference being that the trend of C_P is inverted. Hence, results at high speed appear less sensitive to M, regardless of the under-keel clearance.

The minimum observed for C_P at low speed (Fig. 17, top) can be explained as follows. With Newtonian mud (Mud_23Nwt), the boundary layer is turbulent and thicker than in the water layer because of the increased viscosity (lower Re), as shown in Fig. 18. When using the regularised Bingham with $M = 2000$, the mud viscosity becomes overall larger than with the Newtonian mud, while the effect of the yield stress is still contained. This leads to a laminarised and even thicker boundary

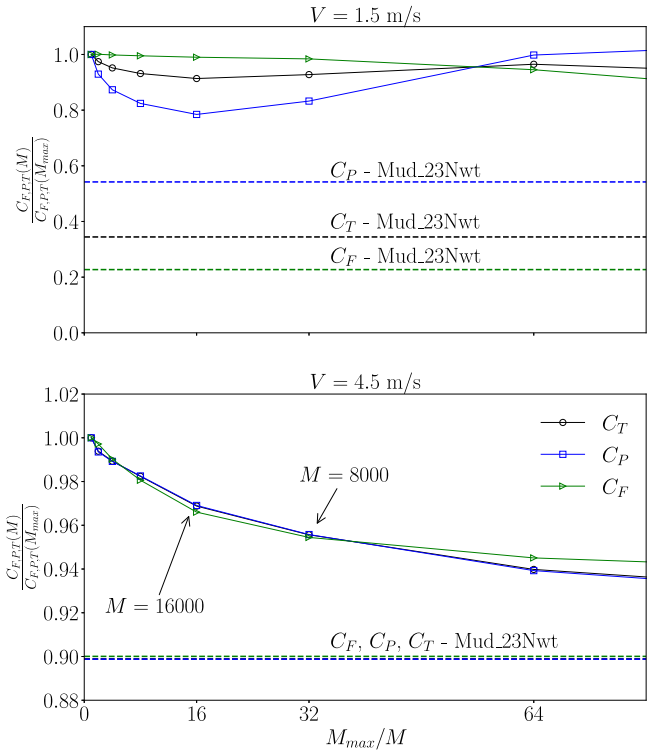

Fig. 17. Effect of regularisation parameter M on the resistance coefficients for the lowest (top) and highest speed (bottom) when sailing through Mud_23 with UKC = −20%. The dashed lines correspond to the calculations with Newtonian mud. M increases from right to left.

layer, which in turn leads to stronger flow separation at the stern and higher pressure resistance. As M is increased further, the influence of the yield stress becomes more pronounced, making the outer flow 'squeeze' the boundary layer towards the wall; the boundary layer becomes thus thinner and flow separation is reduced. This corresponds to the minimum of C_P observed in Fig. 17 (top). With a further increase of M, the boundary layer becomes thinner and thinner and flow separation keeps slightly reducing. However, the effect of the yield stress becomes significant and the pressure component increases again, in analogy with the increase in pressure drag on bluff bodies moving through Bingham fluids (see e.g. Gavrilov et al., 2017; Patel and Chhabra, 2013; Nirmalkar et al., 2013; Lovato et al., 2022c).

In conclusion, $M = 16000$ is adopted for further calculations as it is deemed acceptable to investigate the effect of mud without loss of generality and without compromising the stability of the solver, also keeping in mind that the regularised Bingham model may better describe the flow of real fluid mud. Although using larger values of M may result in slightly different forces, particularly in C_P at low speeds, these differences will not impact the overall conclusions of this study. Nevertheless, the strong sensitivity of C_P to the regularisation parameter at low speeds, both for positive and negative UKC, is revealing and it indicates an alarming sensitivity to the mud rheology. This may be a concern for simulations with non-zero drift angles, where the pressure component can become substantial even at low speeds.

6.2.4. Wall functions

Wall functions are typically used to reduce the number of near-wall cells and thereby the computational costs. In this work, the so-called "automatic" wall functions given in Section 5.3.4 are applied at no-slip boundaries for simulations with negative UKC in order to reduce numerical ventilation, in light of the discussion in Section 6.2.1. However, the adopted wall functions are based on the known near-wall behaviour of attached turbulent flows of Newtonian fluids. Hence, when sailing through non-Newtonian mud, there is no guarantee that, in a mud layer, the wall functions will work as intended.

It was already mentioned in Section 6.2.3 that, with the wall resolved approach and with the considered mud conditions, the flow in the mud layer is laminar when using the Bingham model. Indeed, in that region, it is found that $\mu_t/\mu \ll 1$ even for Mud_10, as shown in Fig. 19(a). Hence, the wall function approach would still be valid in the mud layer if the eddy-viscosity generated at the wall by Eq. (22) remains small compared to the mud viscosity. This occurs if the y^+ on the first cell centroid away from the hull in the mud layer is around or below 1. In general, the lower the mud viscosity, the higher the y^+. In fact, the average y^+ for Mud_10 is about 1.4, whereas for Mud_23 is 0.66. Therefore, the lower the mud viscosity the more refined the near-wall mesh should be in order to keep the y^+ close or below 1.

This also means that Mud_10 represents the worst case; i.e., if the wall functions work correctly for Mud_10, they will also work for with a more viscous mud. Fig. 19(b) shows that, for Mud_10, μ_t/μ is about 0.1 near the bow, but it goes rapidly to zero towards the stern. The resulting C_F at 1.5 m/s is about 3% larger than with the wall-resolved approach, as reported in Table 7. As expected, such difference is smaller for Mud_23. Furthermore, from Table 7 the following observations are made:

- The smallest differences between the wall-resolved and wall function approach are found for the cases without mud. In these cases, the average y^+ on the hull at speeds of 1.5 and 4.5 m/s is about 500 and 1500, respectively, indicating that the first cell is in the "log-layer".
- For the muddy-bottom cases, the wall-function approach leads to substantial over-predictions of C_P at 1.5 m/s. As in Section 6.2.3, the reason seems again the increased flow separation. With wall functions, some eddy-viscosity is artificially generated at the bow (Fig. 19(b)). This increases the overall viscosity of the mud layer, which leads to a slightly thicker boundary layer, which appears to propagate also to the water layer, causing a larger wake at the stern (see Fig. 20).
- At the higher speeds, the use of wall functions does not seem to affect C_P as it is mostly influenced by the internal wave (see also Section 6.3.2). At 4.5 m/s, the ship is mostly in contact with water because of water lubrication (Section 6.2.2), hence the two approaches give fairly similar results.
- With muddy bottoms, large differences in C_F are observed at 3.0 m/s. This is due to numerical ventilation, which significantly reduces the contact area with mud for the wall-resolved simulations, as discussed in Section 6.2.1. In this case, the wall-function approach is deemed more reliable because of the reduced ventilation.

To summarise, the wall-function approach is used in this work for negative UKC in order to reduce numerical ventilation. At low speed, the wall-function approach is expected to over-predict the pressure component, especially for mud layers with lower viscosity. A slightly finer near-wall mesh is expected to reduce such discrepancies.

It is finally remarked that the SST model is not supposed to correctly to capture the flow transition for neither Newtonian nor non-Newtonian fluids. Therefore, it cannot be definitively stated that the flow in the mud layer is laminar without conducting experiments. The objective of this section, on the other hand, was to illustrate the impact of using wall functions and to determine whether they can be effectively used in a non-Newtonian fluid.

6.2.5. Viscosity interpolation in the VOF method

With the large mud undulations occurring at the stern of the ship when sailing at high speeds, small fractions of mud may be suspended into the water layer. Since the viscosity is linearly interpolated between the volume fraction of the two fluids (Eq. (4)), the viscosity in the water

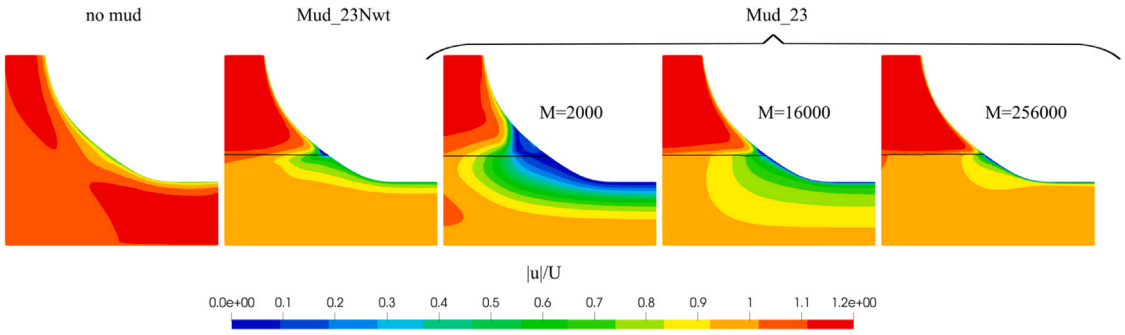

Fig. 18. Velocity magnitude near the hull at $x/L = 0.2$ using different regularisation parameters M when sailing through Mud_23 with UKC = −20% at 1.5 m/s. The black isoline indicates the mud–water interface.

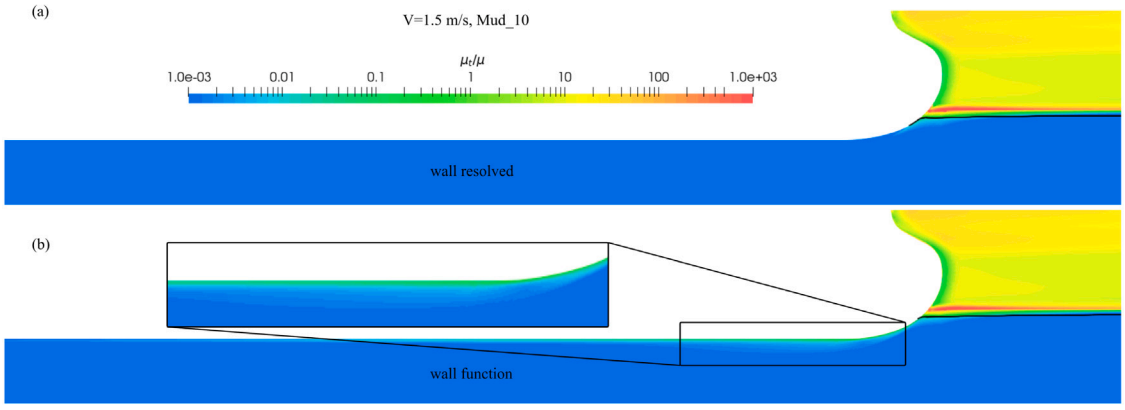

Fig. 19. Ratio of eddy-viscosity over the fluid viscosity with the (a) wall resolved and (b) wall function approach when sailing with UKC = −20% at 1.5 m/s through Mud_10. The black isoline corresponds to the mud–water interface ($c = 0.5$).

Table 7
Resistance coefficient using the wall resolved and the wall function approach on the grid G4. The difference Δ is in percentage of the wall resolved results.

× 1000	C_F	C_P	C_T	C_F	C_P	C_T	C_F	C_P	C_T
	no mud			Mud_10 (UKC = −20%)			Mud_23 (UKC = −20%)		
$V = 1.5$ m/s									
wall resolved	1.987	0.506	2.493	5.782	5.285	11.07	12.17	5.723	17.89
wall function	1.983	0.505	2.488	5.961	6.369	12.33	12.26	6.284	18.55
Δ (%)	−0.22	−0.18	−0.21	3.1	20.5	11.4	0.79	9.8	3.7
$V = 3.0$ m/s									
Wall resolved	1.813	0.451	2.264	1.768	29.67	31.44	2.230	20.42	22.65
Wall function	1.826	0.456	2.282	2.009	29.82	31.83	3.515	20.58	24.10
Δ (%)	0.73	1.09	0.81	13.6	0.52	1.26	57.6	0.80	6.4
$V = 4.5$ m/s									
Wall resolved	1.717	0.422	2.139	1.624	13.69	15.31	1.675	16.38	18.06
Wall function	1.742	0.43	2.172	1.662	13.70	15.36	1.764	16.58	18.35
Δ (%)	1.47	2.05	1.59	2.39	0.10	0.34	5.3	1.2	1.6

layer may increase by orders of magnitude even with just 10% of mud volume-fraction. Although there are correlations that link the sediment concentration to the viscosity, their use would be inconsistent with the VOF method, which assumes immiscible fluids.

A possible approach that is more consistent with the VOF method is to adopt a "sharp" interpolation of the viscosity which would ignore the presence of small fractions of mud in the water layer. For instance, the linear viscosity interpolation given by Eq. (4) could be replaced by the error function (erf):

$$c' = \frac{1}{2}\left\{1 + \mathrm{erf}\left[b(c - 0.5)\right]\right\} \tag{28}$$

$$\mu = \mu_w c' + \mu_m (1 - c') \tag{29}$$

where the steepening coefficient of the error function is chosen as $b = 8$. Fig. 21 shows that even with just 10% of mud ($c = 0.9$) the viscosity is already two orders of magnitude larger than the water viscosity. Using a 'sharper' interpolation mitigates such increase. The benefit of using Eq. (29) is clearly seen in Fig. 22.

However, the erf-type interpolation caused difficulties in the convergence of the iterative solver. These difficulties manifested in larger residuals compared to the linear interpolation method, and in some cases, led to divergence. This is because of the much more abrupt variation of viscosity around the interface. In terms of hull forces, the difference in C_F, C_P and C_T was found to be less than 0.3%. Based on this, it was concluded that while the erf-type interpolation may produce a more realistic viscosity field, it does not provide a significant change in the final results, at least for the considered test cases. Hence, for all subsequent calculations, the viscosity will be calculated with the linear interpolation (Eq. (4)).

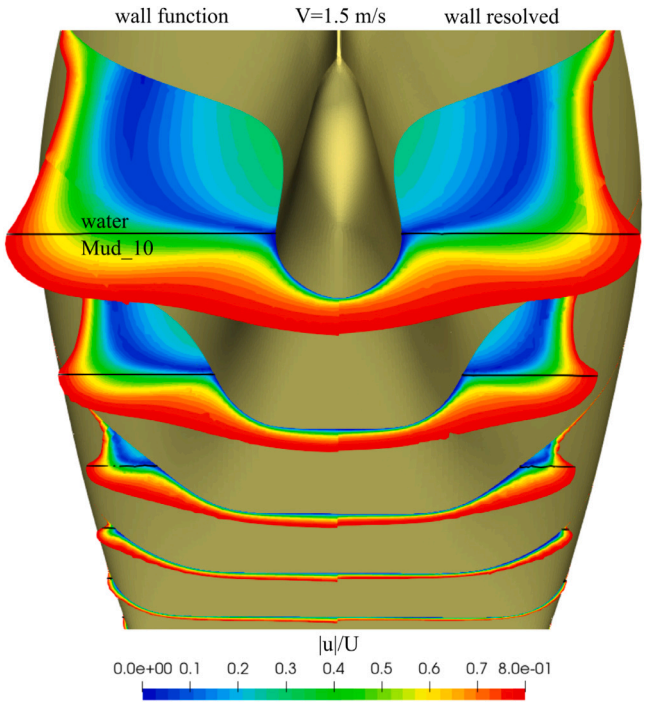

Fig. 20. Fish-view from the stern of the flow for the wall-function (left) and wall-resolved calculations (right) when sailing with UKC = −20% at 1.5 m/s through Mud_10. The black isoline corresponds to the mud–water interface ($c = 0.5$).

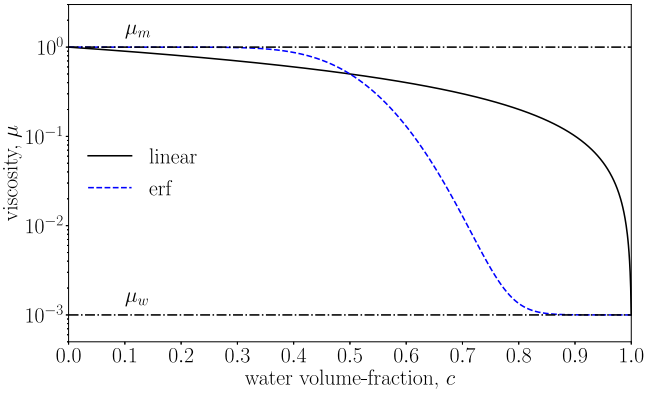

Fig. 21. Viscosity versus the water-volume fraction using linear (Eq. (4)) and an erf-type (Eq. (29)) of interpolation for the viscosity.

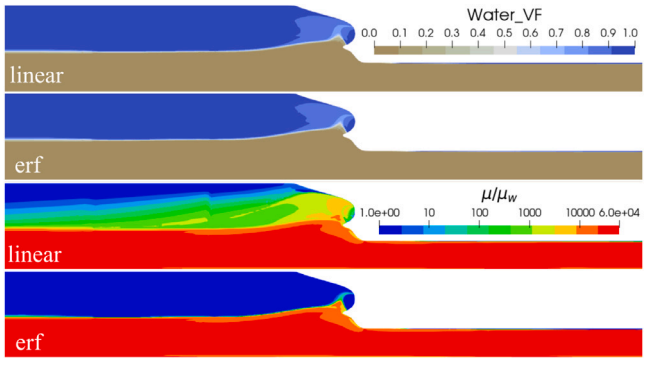

Fig. 22. Contour of (top) water volume-fraction and (bottom) viscosity ratio μ/μ_w at the symmetry plane near the ship's stern at $V = 4.5$ m/s with Mud_23 and UKC = −20%. Flow is from right to left.

6.3. Effect of mud on the resistance

6.3.1. Internal wave pattern

The pressure disturbance generated by the passing ship induces an internal wave on the mud–water interface, both with positive and negative UKC. The wave pattern with UKC = −20% is shown in Fig. 23 for both Mud_10 and Mud_23 at subcritical, transcritical and supercritical densimetric Froude numbers, where the latter was varied by increasing the ship's speed.

In the subcritical range ($Fr_i < 1$), the Kelvin wedge is just barely visible, with the wave elevation being rather small because of the low speed. In the transcritical range ($Fr_i \approx 1$), the angle of the Kelvin wedge increases to up 90 degrees and there is a strong build-up of transverse waves. At such critical speeds, the increase in the resistance can be huge (see Section 6.3.2). In the supercritical range, the transverse waves disappear and only diverging internal waves are visible.

The mud rheology is found to have little impact on the wave pattern. While some differences are observed near critical speeds, these are attributed to the change of Fr_i. As expected, the mud rheology has some effects on the wave elevation, with stronger far-field damping observed for Mud_23.

As a final remark, the internal wave pattern is somewhat analogous to that of free-surface waves in shallow waters but it is also upside-down. For instance, the high pressure at the bow that typically results in a wave elevation of the air–water free surface, hence generating wave crests, pushes the mud–water interface down, thus leading to internal wave troughs.

6.3.2. Effect of the internal wave

The energy needed for a ship to create the internal waves is linked to an increase in the resistance known as "dead-water" phenomenon. When sailing close to a certain critical speed as defined in Section 4.2, i.e. when the densimetric Froude number (Fr_i) is close to 1, a steep increase in C_P occurs (left panel of Fig. 24). This has also been reported in previous studies (Miloh et al., 1993; Zilman and Miloh, 1995; Sano and Kunitake, 2018; Leijs, 2021). No remarkable effects of Fr_i on C_F were observed, hence the focus is limited to C_P.

Regardless of the UKC, C_P appears to be significantly larger than with solid bottoms. However, the influence of the internal wave on C_P is not solely controlled by Fr_i but also by other parameters including speed, under-keel clearance, mud layer thickness and density. (The effects of the rheological properties of mud are left out here and will be discussed in Section 6.3.3.) This also means that the resistance curves against Fr_i are not unique but they rather depend on how Fr_i is varied (e.g. if it is varied by changing V, h_m or ρ_m). The relationship between C_P and these other parameters is not straightforward to illustrate, as changing one parameter affects the others. Despite this, it is postulated that part of the influence of these parameters on the resistance can be related to the amplitude of the internal wave. The total energy of a sinusoidal wave per unit horizontal area reads (Kundu et al., 2015):

$$E_w = \frac{1}{2}(\rho_m - \rho_w) g a_w^2 \tag{30}$$

where a_w is the wave amplitude. Hence, in qualitative terms, the variations of a parameter that lead to an increased amplitude of the internal wave are expected to also increase the resistance.

In mathematical terms, leaving viscous effects aside, the pressure contribution (which contains the main contribution of the internal wave) can be expressed for a given ship and channel depth as follows:

$$C_P = f\left(Fr_i, Fr, \frac{\rho_m}{\rho_w}, \frac{h_m}{T}, \frac{h_w}{T}\right). \tag{31}$$

For a given Fr_i, the above dependency is explained as follows:

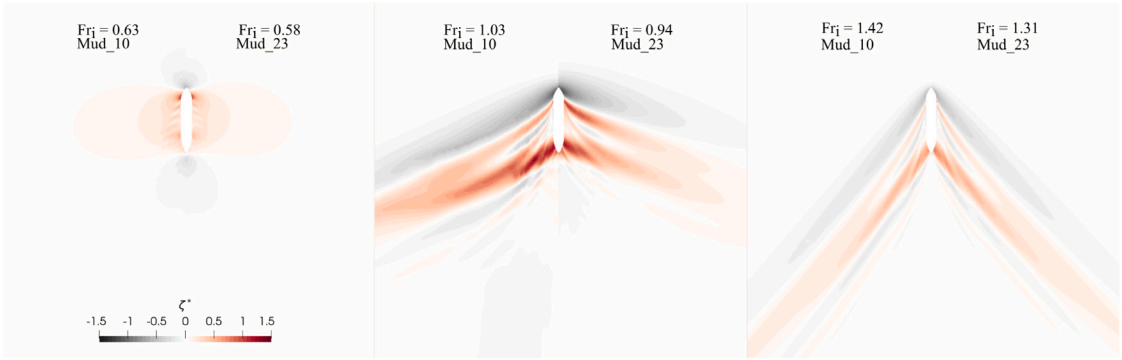

Fig. 23. Contour of the internal (mud) wave elevation ($\zeta^* = \zeta \frac{(1-\rho_1/\rho_2)2g}{V^2}$) at: (left) subcritical, (middle) transcritical and (right) supercritical speeds with UKC = −20%.

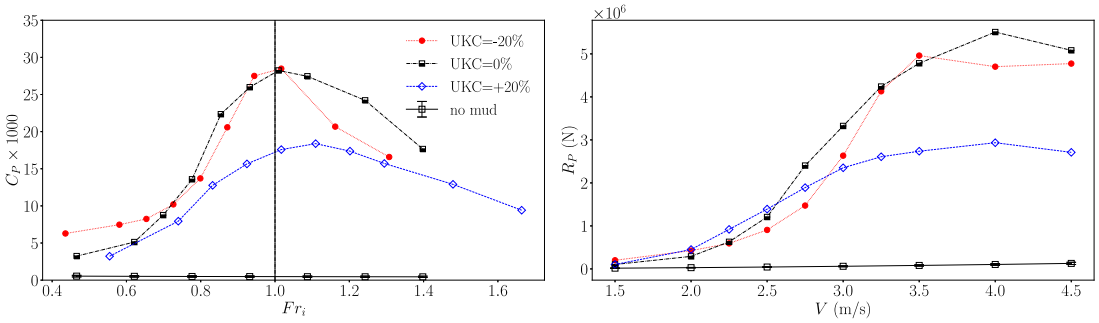

Fig. 24. Effect of UKC on the pressure resistance. All calculations are with Mud_23. Fr_i is varied by changing V. Left: pressure resistance coefficient against the densimetric Froude number. Results without mud are plotted using the Fr_i for UKC = 0%. Right: Pressure resistance against speed.

Fr: With higher speed, the dynamic pressure at the hull increases, which increases the disturbance to the mud–water interface and thereby the wave amplitude. Since the variation of Fr_i in this work has been done by varying the ship's speed, the effect of Fr_i shown in Fig. 24 also implicitly includes the effects of speed.

h_m/T: Generally speaking, a_w cannot exceed h_m, hence larger h_m means potentially larger a_w and therefore higher resistance. This is also consistent with both experimental (Sellmeijer and van Oortmerssen, 1984; Vantorre, 1994), numerical (Sano and Kunitake, 2018) and theoretical observations (Zilman and Miloh, 1995). As a counterexample, Kaidi et al. (2020) showed that the resistance decreases with thicker mud layers. However, h_m was varied by increasing the channel depth while keeping the UKC constant. Hence, in that case, the decrease in resistance is most likely attributable to the reduced shallow-water effects.

h_w/T: This represents the under-keel clearance with respect to the mud–water interface, with $h_w/T = 1$ being equivalent to UKC = 0. Since the hull represents a pressure disturbance, the mud–water interface will feel a stronger disturbance as the UKC approaches zero. Therefore, with zero UKC, more energy is expected to be transferred to the wave system and therefore the resistance will be larger. These can be concisely described as "near-field" or "proximity" effects, which are stronger with small UKC and at higher speeds.

ρ_m/ρ_w: Higher mud density was observed to yield lower wave amplitudes (Sellmeijer and van Oortmerssen, 1984; Vantorre, 1994; Brossard et al., 1991). Intuitively, given the same pressure disturbance, the heavier mud will be less responsive, hence the interface will deform less than with lighter mud. However, a higher mud density will lead to a higher energy content according to Eq. (30), hence the net effect on the resistance is not straightforward. In Zilman and Miloh (1995), the resistance is slightly larger with lower mud densities.

Varying any of the parameters above affects the value of Fr_i, making it difficult to isolate the effect of each parameter. For instance, increasing h_m is expected to enable higher wave amplitudes and therefore larger C_P. However, in practice, other effects also occur: larger h_m implies lower Fr_i, potentially bringing the ship from the super-critical to the trans-critical range, or from the trans-critical to the sub-critical. Furthermore, varying h_m will also alter the UKC, thus influencing the near-field effects. Although the net effect on the pressure resistance is still not easily predicted, these explanations provide both a tool to interpret the results and a warning against making oversimplifications about the link between the resistance and each parameter.

In the example shown in Fig. 24, the UKC is varied from +20% to −20% by increasing h_m. C_P is observed to increase as the UKC decreases from +20% to 0%. This increase is attributed to two factors: the thicker mud layer and the closer proximity of the keel to the interface, which results in greater disturbance of the mud layer. The same increase in C_P is not observed when the UKC is varied from 0 to −20%. Despite the thicker mud layer with negative UKC, the near-field effects are reduced, causing a lower C_P for the case with negative UKC at high speed. This is not true at the lower speeds, where the near-field effects become less important due to the weaker pressure disturbance. At the lowest speed, the variations of C_P are fully ascribed to viscous effects, which are stronger when sailing through mud.

The dimensional pressure resistance, shown in the right panel of Fig. 24, presents a different pattern. In this case, for a given speed, the densimetric Froude number is different for each UKC. At 2.5 m/s, the highest R_P is for UKC = +20% because at that speed the ship is already in the trans-critical range (effect of Fr_i), whereas the other two cases are still sub-critical. For speeds above 3.0 m/s, the cases with zero and positive UKC enter the trans-critical range, where the resistance undergoes a steep increase. At the higher speeds, the cases with zero UKC exhibit the largest R_P due to the stronger proximity effects. Furthermore, the peak of C_P does not directly correspond to a peak of R_P, but rather to a range of speeds in which R_P experiences a steep increase and possibly a local maximum.

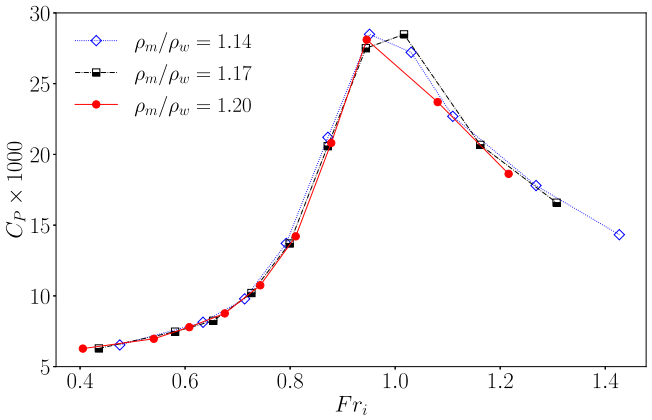

Fig. 25. Effect of mud density on the pressure resistance coefficient against the densimetric Froude number for UKC = −20%. For all calculations, the mud layer has the same τ_B and μ_B of Mud_23.

Finally Fig. 25 illustrates the effect of varying the mud density on C_P. The effect is rather weak but confirms the expectations: for the same Fr_i, i.e. along a vertical line in Fig. 25, the mud with lower density produces a slightly larger C_P, which agrees with the observations in Zilman and Miloh (1995). It is also remarked that for a given Fr_i, the ship's speed is lower for the case with lower density. Yet, even if only slightly, the lower mud density still produces the larger C_P despite the weaker pressure disturbance. In other words, the actual effect of ρ_m/ρ_w alone is stronger than it appears in Fig. 25.

6.3.3. *Effect of the mud rheology*

The influence of the mud rheology on the resistance coefficients is illustrated in Fig. 26 against the densimetric Froude number. The following observations are made:

- In general, the mud rheology is expected to influence the frictional resistance mostly when sailing with negative UKC. While this is confirmed in Fig. 26, a significant influence of the mud rheology is observed only at low speeds. The weak influence of the mud rheology at high speed is in part attributable to numerical ventilation and water lubrication which reduce the contact between the hull and the mud layer (see also Sections 6.2.1 and 6.2.2). For positive UKC, the mud rheology has little influence on friction for the whole investigated speed range. This is also illustrated in the top panel of Fig. 27, where the drop in R_F at intermediate speeds due to water lubrication is clearly visible.
- C_P is rather insensitive to the mud rheology, except that the peak of C_P in the trans-critical range tends to be lower with higher rheological properties and density, especially for UKC = +20%. This can be attributed to both the higher viscous properties and the higher density of Mud_23, as both factors contribute to reduce the amplitude of the undulation. To isolate viscous effects from density effects, one can compare results of Mud_23 and Mud_23Nwt, which share the same density but possess different rheological properties. The comparison indicates that the reduction of the peak is primarily driven by viscous effects. This seems to agree with previous findings (Zilman and Miloh, 1995; Doctors, 1996), where the curve of the resistance coefficient was observed to flatten with increasing mud viscosity.
- When sailing through mud, C_T presents two maxima; one at low speed as a result of the mud yield stress, and the other around $Fr_i = 1$ as a result of the internal waves. When sailing above the mud layer, only the peak due to the internal wave occurs. Compared to the situation without mud, the total resistance with muddy bottoms can become between 2 and 15 times larger.
- For equal Fr_i, the difference in the resistance between Mud_23 and Mud_23Nwt tends to be larger than between Mud_23 and Mud_10. In other words, wrongfully using the Bingham parameters of Mud_10 to simulate Mud_23 is still a better approximation than entirely neglecting the yield stress of Mud_23. Note, however, that this is not true if also the density of Mud_10 is used

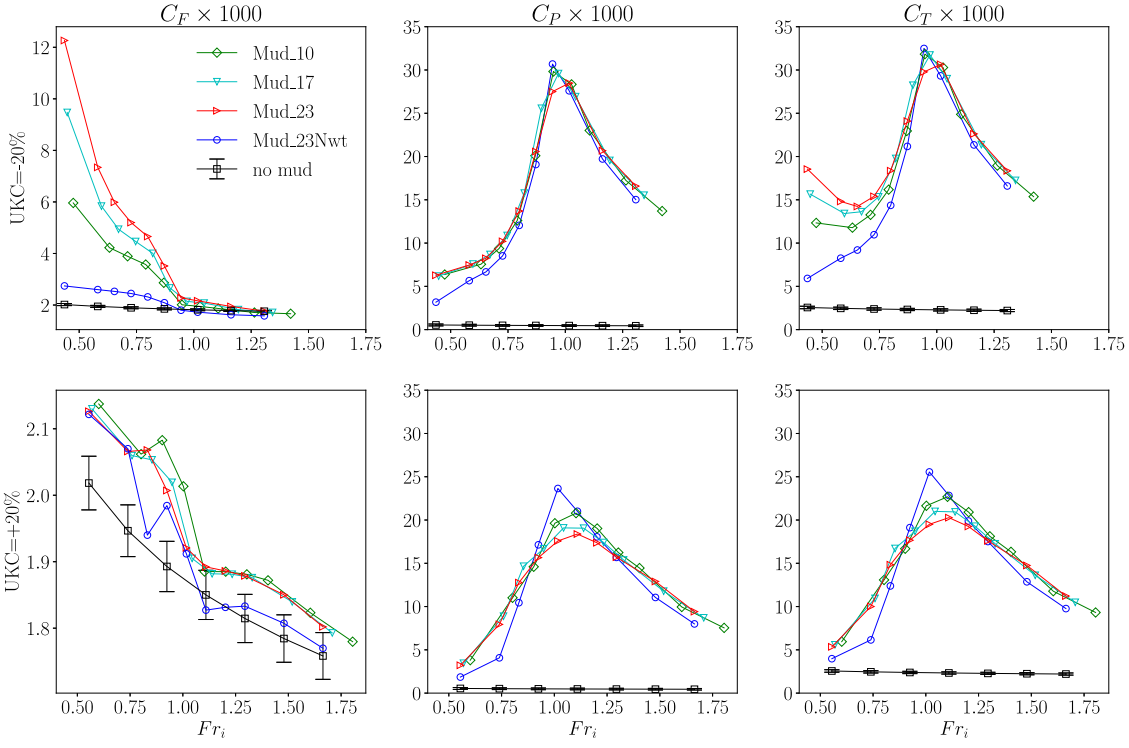

Fig. 26. Resistance coefficients against the densimetric Froude number for different mud conditions and under-keel clearance. Results with no mud are plotted using the densimetric Froude number of Mud_23.

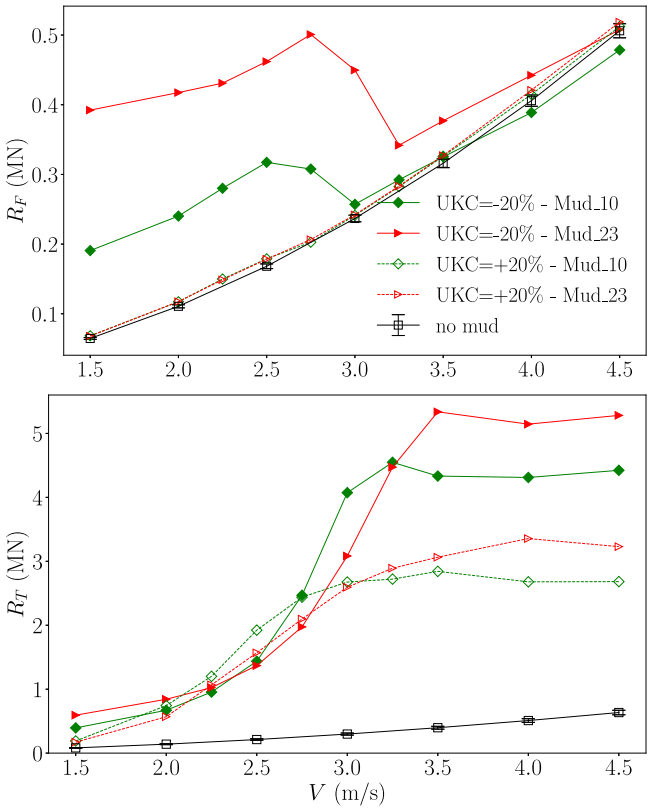

Fig. 27. Effect of mud rheology and UKC on the (top) frictional and (bottom) total resistance against the ship's speed.

as this would alter Fr_i and thereby the influence of the internal wave.

- The frictional coefficient when sailing through a "Bingham" mud at low speed can be simply estimated as:

$$C_F \simeq \overbrace{C_F^0 \frac{S_w}{S}}^{\text{water part}} + \overbrace{\frac{\tau_B}{1/2\rho_w V^2}\left(1 - \frac{S_w}{S}\right)}^{\text{mud part}} \tag{32}$$

where C_F^0 is the friction coefficient without mud, S_w/S is ratio of the hull surface area in contact with water over the total area. When sailing at $V = 1.5$ m/s with UKC $= -20\%$, it is found that $S_w/S = 0.432$ and so Eq. (32) gives 5.80×10^{-3} and 12.2×10^{-3} for Mud_10 and Mud_23, respectively. These values are very close the values obtained from CFD (cf. Table 7). However, as the speed increases, the contact area reduces and the effect of the internal wave are enhanced, making Eq. (32) of little practical use at high speeds.

The R_T curve shown in bottom panel of Fig. 27 is also instructive. The increase in total resistance at low speed with negative UKC appears to be less dramatic than it appears for C_T. Despite the large percentage increase in R_T compared to the case without mud, the increase remains manageable in absolute terms.

R_T appears also to be rather sensitive to the mud rheology even at high speed and with positive UKC, contrary to what was observed for C_T. However, it is remarked that the difference in R_T is actually due to changes in density, which in turn leads to different critical speeds (and Fr_i). Therefore, the differences in R_T are caused by the internal wave rather than the mud rheology. This highlights the importance of keeping track of Fr_i when analysing the effect of mud-related parameters to the dimensional resistance in order to avoid misleading conclusions.

To summarise, a strong link between the mud rheology and the resistance is observed at low speed and with negative UKC, where the increase in resistance due to contact with the mud layer is proportional to the mud yield stress. At the higher speeds, this is no longer true as the influence of the internal wave becomes dominant. Hence, at higher speeds (say, above 2–2.5 m/s), the resistance depends mostly upon the mud layer thickness and density, as these are linked to Fr_i and to the amplitude of the internal wave (see Section 6.3.2).

7. Conclusions and recommendations

A CFD analysis of the full-scale resistance of an oil tanker (KVLCC2) has been carried out for a wide range of speeds and characteristics of the mud layer. The goal was to illustrate the effect of mud layer and its rheology on the resistance. The main conclusions of this work can be summarised as follows:

- The wave-making resistance associated to the internal wave is strongly dependent on the densimetric Froude number, with a very large increase of C_P occurring in the trans-critical range. The results indicate that the resistance is also influenced by other factors such as speed, under-keel clearance, mud layer thickness, and density. This work provides insights into the complex relationship between these parameters and the resistance, and suggests that some of their influence may be linked to the amplitude of the internal waves. Although the exact effect on the resistance is still not easily quantifiable, these insights help to qualitatively anticipate the impact of varying each parameter on the resistance.
- The rheology of mud plays an important role in the force prediction at low speed and with negative UKC. Hence, in these conditions, it is not advisable to entirely neglect the non-Newtonian behaviour of mud.
- Setting the yield stress to zero in the Bingham model to simulate a Newtonian mud layer has a substantial influence on the force prediction, both with positive and negative UKC. Hence, it is not recommended to simulate a Newtonian mud layer by setting its Bingham yield stress to zero. Nonetheless, other strategies to select a suitable molecular viscosity of a Newtonian mud layer may still be viable to obtain acceptable results, but further research is needed.
- When simulating a ship sailing through mud, the frictional forces may be underestimated because of two effects: numerical ventilation and water lubrication. The first can be mitigated by using an artificial correction and by using a coarser near-wall grid in combination with the use of wall functions. The second, on the other hand, is not entirely spurious and it is partly attributed to the expected deformation of the mud–water interface. Nevertheless, adopting different modelling strategies that account for the mixing of mud and water may help minimising water lubrication, but further investigations are still required.
- Using wall functions is a good strategy to reduce computational costs and numerical ventilation. The "automatic" wall function approach can reliably replace the wall-resolved approach also in a non-Newtonian fluid, at least as long as $y^+ < 1$ on the hull portion in contact with the mud layer. Attention should however be paid to cases with stronger flow separation, such as when simulating the ship in manoeuvring conditions.

The calculations were done assuming, among others, that the mud layer is homogeneous and immiscible with water. These are, of course, simplifications of the real-life behaviour of mud layers. Comparing the present results with those obtained with more advanced CFD models that account for mixing and mud stratifications would be very interesting. However, the lack of validation data for this type of problems at the current state would still prevent drawing definitive recommendations about which modelling strategies is best. Furthermore, before considering more advanced modelling techniques, it should be also

kept in mind that, even with such simplifications, CFD simulations with muddy seabeds are already far more expensive than solid-bottom calculations. The reasons for the higher computational costs include the increased number of parameters associated with the mud layer (density, thickness, UKC, rheology), the additional VOF equation to capture the mud–water interface, the extra refinement around the interface, the calculations of the shear-dependent viscosity of mud at each outer iteration and the transient effects associated with the internal wave. Future calculations that include the free surface could clarify the conditions under which the double-body approach remains valid, thereby helping to minimise the computational costs for straight-sailing simulations.

Finally, two interesting extensions of this work would be the analysis of dynamic sinkage and trim and the calculation of the manoeuvring coefficients for a ship sailing through or above fluid mud.

CRediT authorship contribution statement

S. Lovato: Conceptualization, Formal analysis, Investigation, Methodology, Writing – original draft, Writing – review & editing. **S.L. Toxopeus:** Conceptualization, Methodology, Software, Supervision, Writing – original draft, Writing – review & editing. **J.W. Settels:** Conceptualization, Methodology, Supervision, Writing – original draft. **G.H. Keetels:** Funding acquisition, Project administration, Writing – original draft. **A. Kirichek:** Funding acquisition, Project administration, Writing – original draft.

Declaration of competing interest

The authors declare that they have no known competing financial interests or personal relationships that could have appeared to influence the work reported in this paper.

Data availability

Data will be made available on request.

Acknowledgements

This research is funded by the Division for Earth and Life Sciences (ALW) with financial aid from the Netherlands Organization for Scientific Research (NWO) with Grant No. ALWTW.2016.029. Calculations were performed on the Marclus4 (MARIN) cluster. The research support from MARIN is partly funded by the Dutch Ministry of Economic Affairs. This study was carried out within the framework of the MUDNET academic network: https://www.tudelft.nl/mudnet/.

Appendix A. SST model

The details of the $k-\omega$ SST model of Menter et al. (2003) used in this work are reported below.

$$F_1 = \tanh\left\{ \min\left[\max\left(\frac{\sqrt{k}}{\beta^* \omega d}, \frac{500\nu}{d^2\omega} \right), \frac{4\rho\sigma_{\omega 2} k}{CD_{k\omega} d^2} \right]^4 \right\} \tag{A.1}$$

d is the distance to the wall boundary.

$$CD_{k\omega} = \max\left(2\rho\sigma_{\omega 2} \frac{1}{\omega} \nabla k \cdot \nabla\omega, 10^{-10} \right) \tag{A.2}$$

$$\mu_t = \frac{\rho_1 k}{\max(a_1\omega, \dot{\gamma} F_2)}, a_1 = 0.31, \dot{\gamma} = \sqrt{2 S_{ij} S_{ij}} \tag{A.3}$$

$$F_2 = \tanh\left\{ \left[\max\left(\frac{2\sqrt{k}}{\beta^* \omega d}, \frac{500\mu}{d^2 \rho\omega} \right) \right]^2 \right\} \tag{A.4}$$

$$\tilde{P}_k = \min(\mu_t \dot{\gamma}^2, 10\beta^* \rho k\omega), \beta^* = 0.09 \tag{A.5}$$

$$\alpha = \alpha_1 F_1 + (1 - F_1)\alpha_2, \quad \beta = \beta_1 F_1 + (1 - F_1)\beta_2,$$
$$\sigma_k = \sigma_{k1} F_1 + (1 - F_1)\sigma_{k2}, \quad \sigma_\omega = \sigma_{\omega 1} F_1 + (1 - F_1)\sigma_{\omega 2},$$
$$\alpha_1 = 5/9, \quad \beta_1 = 3/40, \quad \sigma_{k1} = 0.85, \quad \sigma_{\omega 1} = 0.5,$$
$$\alpha_2 = 0.44, \quad \beta_2 = 0.0828, \quad \sigma_{k2} = 1, \quad \sigma_{\omega 2} = 0.856.$$

Appendix B. Supplementary data

Supplementary material related to this article can be found online at https://doi.org/10.1016/j.oceaneng.2024.116700.

References

Avci, A.G., Barlas, B., 2018. An experimental and numerical study of a high speed planing craft with full-scale validation. J. Mar. Sci. Technol. 26 (5), 617–628, URL https://jmstt.ntou.edu.tw/journal/vol26/iss5/1.

Barth, R., van der Made, C.J.A.W., Bourgonjen, L., van Dijken, J., Vantorre, M., Verwilligen, J., 2016. Manoeuvring with negative underkeel clearance: 2nd full scale field test in the port of Delfzijl. In: 4th MASHCON-International Conference on Ship Manoeuvring in Shallow and Confined Water with Special Focus on Ship Bottom Interaction. pp. 262–271.

Brossard, C., Delouis, A., Galichon, P., Granboulan, J., Monadier, P., 1991. Navigability in channels subject to siltation physical scale model experiments. In: 22nd International Coastal Engineering Conference. Delft, the Netherlands, American Society of Civil Engineers, pp. 3088–3101. http://dx.doi.org/10.1061/9780872627765.236.

Chhabra, R.P., Richardson, J.F., 2008. Non-Newtonian Flow and Applied Rheology. Elsevier, p. 536. http://dx.doi.org/10.1016/B978-0-7506-8532-0.X0001-7.

Coussot, P., 2017. Mudflow Rheology and Dynamics. Routledge, http://dx.doi.org/10.1201/9780203746349.

Crepier, P., 2017. Ship resistance prediction: Verification and validation exercise on unstructured grids. In: MARINE VII: Proceedings of the VII International Conference on Computational Methods in Marine Engineering. pp. 365–376.

Delefortrie, G., Vantorre, M., Eloot, K., 2005. Modelling navigation in muddy areas through captive model tests. J. Mar. Sci. Technol. 10 (4), 188–202. http://dx.doi.org/10.1007/s00773-005-0210-5.

Delefortrie, G., Vantorre, M., Verzhbitskaya, E., Seynaeve, K., 2007. Evaluation of safety of navigation in muddy areas through real-time maneuvering simulation. J. Waterw. Port Coast. Ocean Eng. 133 (2), 125–135. http://dx.doi.org/10.1061/(ASCE)0733-950X(2007)133:2(125).

Doctors, L.J., 1996. The influence of a bottom mud layer on the steady-state hydrodynamics of marine vehicles. In: 21st Symposium on Naval Hydrodynamics. National Academies Press, pp. 727–742.

Dzuy, N.Q., Boger, D.V., 1985. Direct yield stress measurement with the vane method. J. Rheol. 29 (3), 335–347. http://dx.doi.org/10.1122/1.549794.

Eça, L., Hoekstra, M., 2009. Evaluation of numerical error estimation based on grid refinement studies with the method of the manufactured solutions. Comput. & Fluids 38 (8), 1580–1591. http://dx.doi.org/10.1016/j.compfluid.2009.01.003.

Eça, L., Hoekstra, M., 2014. A procedure for the estimation of the numerical uncertainty of CFD calculations based on grid refinement studies. J. Comput. Phys. 262, 104–130. http://dx.doi.org/10.1016/j.jcp.2014.01.006.

Eça, L., Pereira, F.S., Vaz, G., 2018. Viscous flow simulations at high Reynolds numbers without wall functions: Is $y^+ \simeq 1$ enough for the near-wall cells? Comput. & Fluids 170, 157–175. http://dx.doi.org/10.1016/j.compfluid.2018.04.035.

Ekman, V.W., 1904. On dead water. In: Norwegian North Polar Expedition, 1893-1896. pp. 1–150.

Ellwood, K.R.J., Georgiou, G.C., Papanastasiou, T.C., Wilkes, J.O., 1990. Laminar jets of Bingham-plastic liquids. J. Rheol. 34 (6), 787–812. http://dx.doi.org/10.1122/1.550144.

Esmaeilpour, M., Ezequiel Martin, J., Carrica, P.M., 2018. Computational fluid dynamics study of the dead water problem. J. Fluids Eng. 140 (3), http://dx.doi.org/10.1115/1.4037693.

Gao, Z., Yang, H., Xie, M., 2015. Computation of flow around Wigley Hull in shallow water with muddy seabed. J. Coast. Res. 73, 490–495. http://dx.doi.org/10.2112/SI73-086.1.

Gavrilov, A.A., Finnikov, K.A., Podryabinkin, E.V., 2017. Modeling of steady Herschel–Bulkley fluid flow over a sphere. J. Eng. Thermophys. 26 (2), 197–215. http://dx.doi.org/10.1134/S1810232817020060.

Goeree, J.C., Keetels, G.H., Munts, E.A., Bugdayci, H.H., van Rhee, C., 2016. Concentration and velocity profiles of sediment-water mixtures using the drift flux model. Can. J. Chem. Eng. 94 (6), 1048–1058. http://dx.doi.org/10.1002/cjce.22491.

Gray-Stephens, A., Tezdogan, T., Day, S., 2021. Minimizing numerical ventilation in computational fluid dynamics simulations of high-speed planning hulls. J. Offshore Mech. Arct. Eng. 143 (3), http://dx.doi.org/10.1115/1.4050085.

Grue, J., 2015. Nonlinear dead water resistance at subcritical speed. Phys. Fluids 27 (8), 082103. http://dx.doi.org/10.1063/1.4928411.

Hino, T., 2005. in: CFD Workshop Tokyo 2005. National Maritime Research Institute, Tokyo.

Hirt, C.W., Nichols, B.D., 1981. Volume of fluid (VOF) method for the dynamics of free boundaries. J. Comput. Phys. 39 (1), 201–225. http://dx.doi.org/10.1016/0021-9991(81)90145-5.

Irgens, F., 2014. Rheology and Non-Newtonian Fluids. Springer International Publishing, Cham, pp. 1–190. http://dx.doi.org/10.1007/978-3-319-01053-3.

Kaidi, S., Lefrançois, E., Smaoui, H., 2020. Numerical modelling of the muddy layer effect on ship's resistance and squat. Ocean Eng. 199, 106939. http://dx.doi.org/10.1016/j.oceaneng.2020.106939.

Klaij, C.M., Hoekstra, M., Vaz, G., 2018. Design, analysis and verification of a volume-of-fluid model with interface-capturing scheme. Comput. & Fluids 170, 324–340. http://dx.doi.org/10.1016/j.compfluid.2018.05.016.

Klaij, C.M., Vuik, C., 2013. SIMPLE-type preconditioners for cell-centered, colocated finite volume discretization of incompressible Reynolds-averaged Navier-Stokes equations. Internat. J. Numer. Methods Fluids 71 (7), 830–849. http://dx.doi.org/10.1002/fld.3686.

Kundu, P.K., Cohen, I.M., Dowling, D.R., 2015. Fluid Mechanics, Volume 10. Academic Press, (ISSN: 0009-4978) ISBN: 9780124071513, URL https://www.elsevier.com/books/fluid-mechanics/kundu/978-0-12-405935-1.

Larsson, L., Stern, F., Bertram, V., 2003. Benchmarking of computational fluid dynamics for ship flows: The Gothenburg 2000 workshop. J. Ship Res. (ISSN: 00224502) 47 (1), http://dx.doi.org/10.5957/jsr.2003.47.1.63.

van Leer, B., 1979. Towards the ultimate conservative difference scheme. V. A second-order sequel to Godunov's method. J. Comput. Phys. 32 (1), 101–136. http://dx.doi.org/10.1016/0021-9991(79)90145-1.

Leijs, K., 2021. CFD Simulations of the Flow Around a Tanker in Shallow Water with Muddy Seabed (MSc thesis). Delft University of Technology, Delft, The Netherlands, URL http://resolver.tudelft.nl/uuid:a7c7e1ae-e7f0-4e15-9a03-0901af9e8959.

Lovato, S., 2023. Sailing Through Fluid Mud: Verification and Validation of a CFD Model for Simulations of Ships Sailing in Muddy Areas (Ph.D. thesis). Delft University of Technology, Delft, ISBN: 978-94-6458-954-2, pp. 1–219. http://dx.doi.org/10.4233/uuid:b2156264-39f4-4a8d-a34d-35e5a21d38e9.

Lovato, S., Keetels, G.H., Toxopeus, S.L., Settels, J.W., 2022a. An eddy-viscosity model for turbulent flows of Herschel–Bulkley fluids. J. Non-Newton. Fluid Mech. 301, 104729. http://dx.doi.org/10.1016/j.jnnfm.2021.104729.

Lovato, S., Kirichek, A., Toxopeus, S.L., Settels, J.W., Keetels, G.H., 2022b. Validation of the resistance of a plate moving through mud: CFD modelling and towing tank experiments. Ocean Eng. 258, 111632. http://dx.doi.org/10.1016/j.oceaneng.2022.111632.

Lovato, S., Toxopeus, S.L., Settels, J.W., Keetels, G.H., 2022c. Application of a maritime CFD code to a benchmark problem for non-Newtonian fluids: The flow around a sphere. Int. Shipbuild. Prog. 70 (1), 1–25. http://dx.doi.org/10.3233/ISP-220002.

Lovato, S., Toxopeus, S.L., Settels, J.W., Keetels, G.H., Vaz, G., 2021. Code verification of non-Newtonian fluid solvers for single- and two-phase laminar flows. J. Verification Valid. Uncertain. Quantif. 6 (2), http://dx.doi.org/10.1115/1.4050131.

McAnally, W.H., Teeter, A., Schoellhamer, D., Friedrichs, C., Hamilton, D., Hayter, E., Shrestha, P., Rodriguez, H., Sheremet, A., Kirby, R., 2007. Management of fluid mud in estuaries, bays, and lakes. II: Measurement, modeling, and management. J. Hydraul. Eng. 133 (1), 23–38. http://dx.doi.org/10.1061/(ASCE)0733-9429(2007)133:1(23).

McBride, M., Boll, M., Briggs, M., 2014. Harbour Approach Channels—Design Guidelines. PIANC, Brussels, Belgium.

Menter, F.R., 1994. Two-equation eddy-viscosity turbulence models for engineering applications. AIAA J. 32 (8), 1598–1605. http://dx.doi.org/10.2514/3.12149.

Menter, F.R., Kuntz, M., Langtry, R., 2003. Ten years of industrial experience with the SST turbulence model turbulence. Turbulence, Heat and Mass Transfer 4.

Mercier, M.J., Vasseur, R., Dauxois, T., 2011. Resurrecting dead-water phenomenon. Nonlinear Process. Geophys. 18 (2), 193–208. http://dx.doi.org/10.5194/npg-18-193-2011.

Millward, A., 1989. The effect of water depth on hull form factor. Int. Shipbuild. Prog. 36 (407), 283–302.

Miloh, T., 1995. Ship motion in non-homogeneous media. Ship Technol. Res. (ISSN: 09377255) 42 (3).

Miloh, T., Tulin, M.P., Zilman, G., 1993. Dead-water effects of a ship moving in stratified seas. J. Offshore Mech. Arct. Eng. 115 (2), 105–110. http://dx.doi.org/10.1115/1.2920098.

Nansen, F., 2008. Farthest North: The Epic Adventure of a Visionary Explorer. Skyhorse Publishing Inc..

Nirmalkar, N., Chhabra, R.P., Poole, R.J., 2013. Laminar forced convection heat transfer from a heated square cylinder in a Bingham plastic fluid. Int. J. Heat Mass Transfer 56 (1–2), 625–639. http://dx.doi.org/10.1016/j.ijheatmasstransfer.2012.08.049.

Ouda, M., Toorman, E.A., 2019. Development of a new multiphase sediment transport model for free surface flows. Int. J. Multiph. Flow 117, 81–102. http://dx.doi.org/10.1016/j.ijmultiphaseflow.2019.04.023.

Papanastasiou, T.C., 1987. Flows of materials with yield. J. Rheol. 31 (5), 385–404. http://dx.doi.org/10.1122/1.549926.

Patel, S.A., Chhabra, R.P., 2013. Steady flow of Bingham plastic fluids past an elliptical cylinder. J. Non-Newton. Fluid Mech. 202, 32–53. http://dx.doi.org/10.1016/j.jnnfm.2013.09.006.

Pereira, F.S., Eça, L., Vaz, G., 2017. Verification and validation exercises for the flow around the KVLCC2 tanker at model and full-scale Reynolds numbers. Ocean Eng. 129, 133–148. http://dx.doi.org/10.1016/j.oceaneng.2016.11.005.

Sano, M., Kunitake, Y., 2018. Numerical solution for a ship-wave problem in a two-layer fluid using a double-model linearised interface condition. Ships Offshore Struct. 13 (3), 293–302. http://dx.doi.org/10.1080/17445302.2017.1371391.

Sellmeijer, R., van Oortmerssen, G., 1984. The effect of mud on tanker manoeuvres. R. Inst. Nav. Archit. Trans. 126.

Sotelo, M.S., Boucetta, D., van Hoydonck, W., Doddugollu, P., Vantorre, M., Toorman, E., Delefortrie, G., 2023. Hydrodynamic forces acting on a cylinder towed in muddy environments. J. Waterw. Port Coast. Ocean Eng. 149 (6), http://dx.doi.org/10.1061/JWPED5.WWENG-1992.

Syrakos, A., Georgiou, G.C., Alexandrou, A.N., 2013. Solution of the square lid-driven cavity flow of a Bingham plastic using the finite volume method. J. Non-Newton. Fluid Mech. 195, 19–31. http://dx.doi.org/10.1016/j.jnnfm.2012.12.008.

Toxopeus, S.L., 2013. MARINE 2011, IV international conference on computational methods in marine engineering: Viscous-flow calculations for KVLCC2 in deep and shallow water. In: Computational Methods in Applied Sciences, Springer, pp. 151–169. http://dx.doi.org/10.1007/978-94-007-6143-8_9.

Van Bochove, G., Nederlof, L., 1978. Vaargedrag van diepstekende schepen in slibrijke gebieden. Ingenieur 91 (30/31), 525–530.

Van Craenenbroeck, K., Vantorre, M., De Wolf, P., 1992. Navigation in muddy areas: Establishing the navigagable depth in the port of Zeebrugge. In: CEDA-PIANC Conference. PIANC.

Van Hoydonck, W., Toxopeus, S., Eloot, K., Bhawsinka, K., Queutey, P., Visonneau, M., 2019. Bank effects for KVLCC2. J. Mar. Sci. Technol. (ISSN: 0948-4280) 24 (1), 174–199. http://dx.doi.org/10.1007/s00773-018-0545-3.

Vantorre, M., 1994. Ship behaviour and control in muddy areas: State of the art. In: 3rd International Conference on Manoeuvring and Control of Marine Craft. MCMC '94, Southampton, UK.

Vantorre, M., Coen, I., 1988. On sinkage and trim of vessels navigating above a mud layer. In: The Royal Society of Flemish Engineers, Harbour Congress.

Vaz, G., Jaouen, F., Hoekstra, M., 2009. Free-surface viscous flow computations: Validation of URANS code FRESCO. In: Proceedings of OMAE 2009. Honolulu, Hawaii, USA, pp. 425–437. http://dx.doi.org/10.1115/OMAE2009-79398.

Verwilligen, J., Vantorre, M., Delefortrie, G., Meinsma, J., van der Made, K.J., 2014. Manoeuvrability in proximity of nautical bottom in the harbour of Delfzijl. In: 33rd PIANC World Congress. PIANC, pp. 1–18.

Viola, I.M., Flay, R.G.J., Ponzini, R., 2012. CFD analysis of the hydrodynamic performance of two candidate America's cup AC33 hulls. Trans. R. Inst. Nav. Archit. B 154 (1), http://dx.doi.org/10.3940/rina.ijsct.2012.b1.113.

Windt, J., 2013. Adaptive mesh refinement in viscous flow solvers: Refinement in the near-wall region, implementation and verification. In: 16th NuTTS. Müllheim, Germany, pp. 171–176.

Yeung, R.W., Nguyen, T.C., 1999. Waves generated by a moving source in a two-layer ocean of finite depth. J. Engrg. Math. 35 (1–2), http://dx.doi.org/10.1023/a:1004399917692.

Zeng, Q., Hekkenberg, R., Thill, C., 2019. On the viscous resistance of ships sailing in shallow water. Ocean Eng. 190, 106434. http://dx.doi.org/10.1016/j.oceaneng.2019.106434.

Zilman, G., Kagan, L., Miloh, T., 1996. Hydrodynamics of a body moving over a mud layer - Part II: Added-mass and damping coefficients. J. Ship Res. 40 (1), 39–45. http://dx.doi.org/10.5957/jsr.1996.40.1.39.

Zilman, G., Miloh, T., 1995. Hydrodynamics of a body moving over a mud layer - Part I: Wave resistance. J. Ship Res. (ISSN: 00224502) 39 (3).